SASE FEL at the TESLA Facility, Phase 2

Abstract

The last description of the TESLA Test Facility FEL has been written in 1995 (TESLA-FEL report 95-03). Since then, many changes have developed compared to the design, partially because the design was incomplete, partly because of gained knowledge over the past few years. In addition, what used to be known as phase II of the project has been subdivided into a finer time scale, starting with the first beam through the machine until the complete user facility with its different possible extensions.

This report is therefore an upgrade of the above mentioned Conceptual Design Report. It is by no means complete or final, but gives a more complete overview of the present status of knowledge on present and future developments towards the TTF-FEL user facility.

1 Introduction

Phase 2 of the TESLA Test Facility (TTF-2) is planned as a user facility for soft X-ray FEL radiation. The design energy of the electron beam is 1 GeV, corresponding to a radiation wavelength of 6.4 nm or 194 eV photon energy. The machine upgrade for TTF-2 is much more than a simple extension of the accelerator by a few additional ”modules”. It includes a number of modifications in order to deliver the electron beam quality required for short wavelengths and to ensure reliable operation for the FEL user facility.

The schematic layout of TTF-2 is shown in Fig. 1. The electron beam is produced in an RF gun and accelerated up to 1 GeV by six cryomodules, each containing eight superconducting RF cavities and a quadrupole doublet. At energy levels of 130 MeV and 440 MeV the electron bunches are compressed from a length of 2 mm RMS at the exit of the gun to approximately 50 μm RMS in order to provide a peak current of 2.5 kA required for the FEL. A collimator section protects the FEL undulator by removing particles with an energy deviation larger than $\pm 3\%$ and with large betatron amplitudes. It is also possible to bypass the complete FEL area in order to facilitate machine commissioning and the test of accelerator components. Finally, a dipole magnet deflects the electron beam into a dump, while the FEL radiation propagates to the experimental hall.

This report is an upgrade of the TTF-FEL Conceptual Design Report [1], describing the main changes with respect to the original design. It is not intended to give a complete overview of the machine, which can be found in Ref. [1]. Neither is it a complete technical report. Details on components and parts of the machine are documented in the many technical reports and publications of the past years. Most of them can be found at

http://tesla. desy.de/new_pages/5114_FEL_reports.html

However, at the time when the original design of the TTF-FEL was published, many details were not yet known. In addition, operation of the present (phase-1) FEL, has shown how several parts could be changed to improve of simplify the operation for the (expected) design parameters of phase-2.

The report is organized as follows. Section 2 is dedicated to the injector. In section 3,the bunch compressor system is discussed. Section 4 discusses the beam dynamics in the linac section, section 5 the collimator and section 6 the electron beam diagnostics to measure the phase space. In section 7 the modified undulator setup with diagnostics is discussed. New in this report is the experimental user area, which is discussed in section 8. Because the route to short radiation wavelengths is now much better known and because of the experience obtained during operation of the TTF-FEL over the past years, a more detailed discussion of photon beam parameters that will be available for users is discussed in section 9.

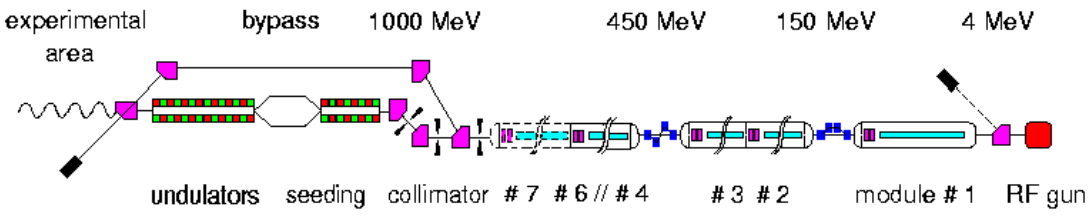


Fig. 1. *Schematic layout of TTF-2*

2 Injector

2.1 Introduction and basic principle

Both small emittance values and high phase space density in all three dimensions are mandatory for achieving micro-bunching and saturation within an undulator of reasonable length. To achieve a photon wavelength λ, the transverse normalized emittance $\tilde{\varepsilon}_\perp$ must not exceed a critical value given by:

$$\tilde{\varepsilon}_\perp \sim p_z \lambda/(4\pi mc),$$

where p_z is the longitudinal momentum. Since in a linac no radiative damping occurs and the emittance generally tends to increase (e.g. due to collective force within the bunch), the electron bunches have to be produced at the gun with an emittance smaller than the specified one at the undulator.

RF-guns based on photo-emission [2] allow the production of such high phase space density beams. In an RF-gun electrons are photo-emitted from a cathode which is placed in the back plane of the half-cell of an RF-cavity. Hence electrons experience a very high accelerating E-field from the very beginning (at TTF-1 such field is typically 40 MV/m) and are rapidly accelerated. The transverse emittance is affected by several contributions:

(1) the initial thermal emittance coming from the emission process,
(2) the RF-induced emittance (due to the time dependence of the RF-field radial (focusing) component,
(3) linear and nonlinear space charge forces.

The contributions (1) and (2) depend on the laser beam spot size on the photocathode. The linear space charge force (in contribution (3)) can be removed using the so-called emittance compensation process [3]. This technique for the compensation of correlated emittance contributions has been experimentally demonstrated at the Accelerator Test Facility (ATF) at BNL [4]. The underlying argument for such a compensation mechanism is as follows (see Fig. 2): In an RF gun, operating in the space charge dominated regime, most of the emittance growth is due to the space charge forces, which introduce correlations between the phase space r, p_r and the longitudinal position z (i.e. the space charge field variation along z results in different transverse betatron phase advances for different longitudinal slices of the bunch). Typically the space charge field is stronger in the longitudinally central slices than towards the ends of the bunch. Correspondingly the center slices will have a higher radial momentum p_r. With a properly tuned solenoid it is possible to introduce a focusing kick which will, after a drift of proper length in which the space charge force acts again, result in a cancellation of the correlation induced by space charge.

After reaching a minimum, the emittance would grow again under the influence of the space charge in a drift section. To circumvent this, the final stage of the compensation process has to take place in an accelerating section, so that the minimum emittance is reached at higher energy where the space charge force is sufficiently suppressed.

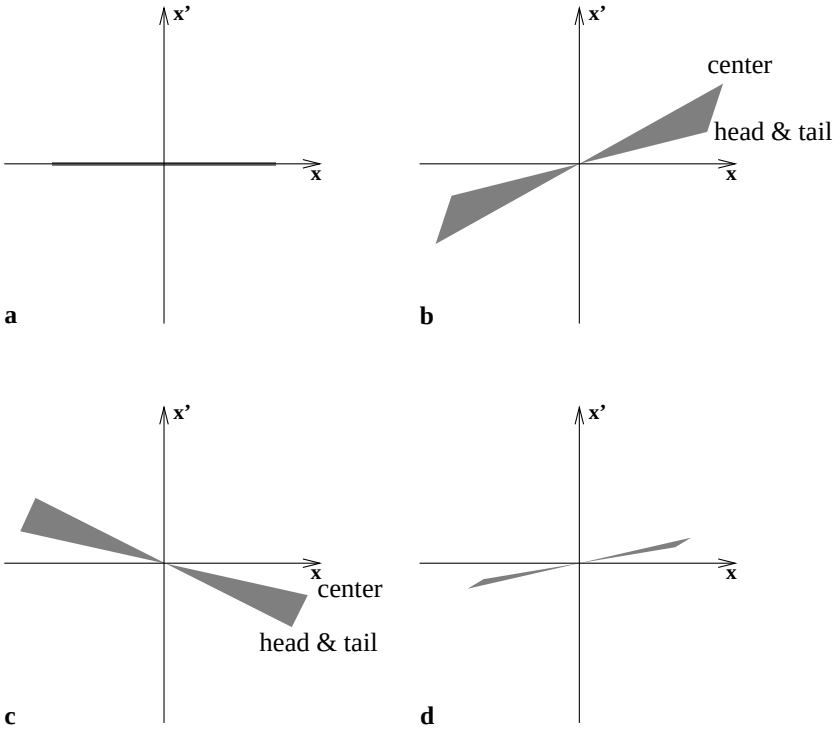


Fig. 2. Transverse phase space plots showing schematically transverse emittance growth and reduction due to space charge forces. (a) Initial phase space with small (zero) emittance at the gun. (b) Phase space after transport up to the solenoid lens, showing the growth of the projected emittance due to the different focusing strength at the bunch center and the tails. (c) The phase space distribution has been rotated by an external focusing kick. (d) Phase space after a drift behind the lens. The projected emittance is decreased due to the action of the space charge forces.

2.2 The electron source

The gun section is composed of a 1+1/2 cell photoemission based RF gun (f =1.3 GHz) and a solenoid lens followed by a drift of proper length to allow the emittance compensation process to take place. A bucking coil behind the gun compensates the solenoid field at the cathode position. The gun cavity with the solenoids is sketched in Fig. 3 – the corresponding electric and magnetic on-axis field profiles are shown in Fig. 4. The RF gun consists of a cylindrically symmetric cavity with an on-axis coaxial RF coupler [5]. The on-axis coupler avoids RF field asymmetries (dipole and higher order) which can lead to a significant emittance growth. Similarly to the Tesla Test Facility (TTF) injector, Cs_2Te photocathodes [6] will be employed, illuminated by a laser with a wavelength of 262 nm. Given the quantum efficiency of Cs_2Te photocathodes ($\sim$0.5%), 1 μJ of UV laser energy is sufficient to produce the required maximum charge of 1 nC. A sufficient reserve to produce even higher charges (up to 4 nC) will be provided. The laser will generate variable pulse structures (see Table 1). Since the maximum number of pulses per bunch train is 7200, the total laser energy should be $\sim$ 6 mJ per train. For a train repetition rate of 10 Hz, an average power of 55 mW is required. Most of these requirements have already been achieved at the TTF [7]. The laser should produce a radially and longitudinally uniform photon density on the photocathode. This type of distribution is preferred for the reduced impact on the beam emittance, since the transverse space charge forces within the bunch remain linear. An upgrade of the TTF-1 laser will bring the rise time close to the required values of 2 ps. A

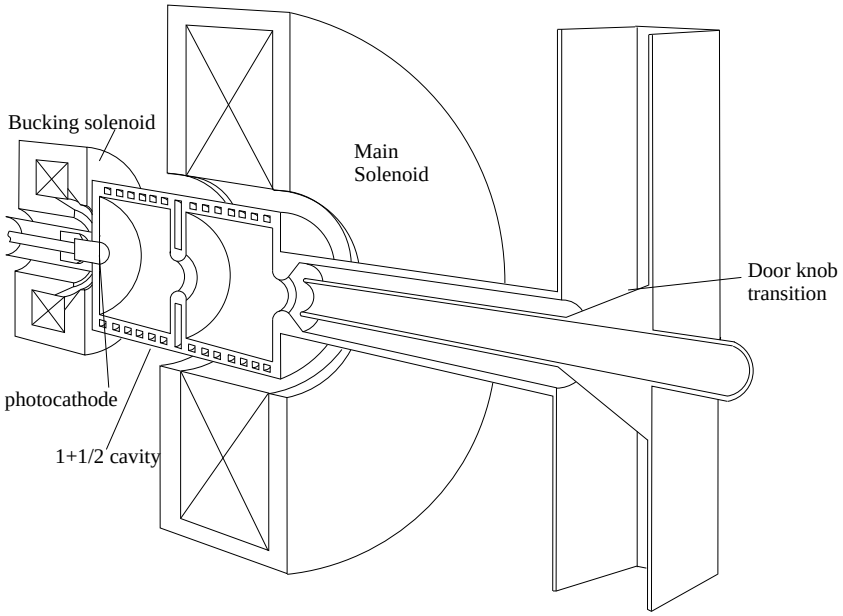


Fig. 3. *Cross sectional view of the RF gun along with the main and bucking solenoid and the RF input coupler.*

substantial upgrade will be the possibility to stack these short pulses using an interferometric pulse stacker: such a feature will enable the generation of a "flat-top"-like time-distribution.

Wavelength	262 nm
Energy on photocathode/bunch	$\sim$1 μJ
Train rep. rate	10 Hz
Pulse train length (max.)	800 μm
Nb. of bunches per train (max.)	7200
Pulse spacing (min.)	111 ns

Table 1
Requirements on the photoinjector laser.

2.3 Accelerating section

Downstream of the gun, a standard TESLA accelerating module accelerates the beam up to 130 MeV. The first four cavities of the module provide an average gradient of $G_{RF} \simeq 12.5$ MV/m, whereas the last four cavities are operated at full performance (assumed to be $G_{RF} = 20$ MV/m). Following this accelerating section, a 3.9 GHz accelerating section is used to correct the distortion in the longitudinal phase space (see next section). A plot of the emittance compensation process and damping during the acceleration is presented in figure 5. The transverse emittance achieved after acceleration is 1.2 mm-mrad (this number includes thermal emittance).

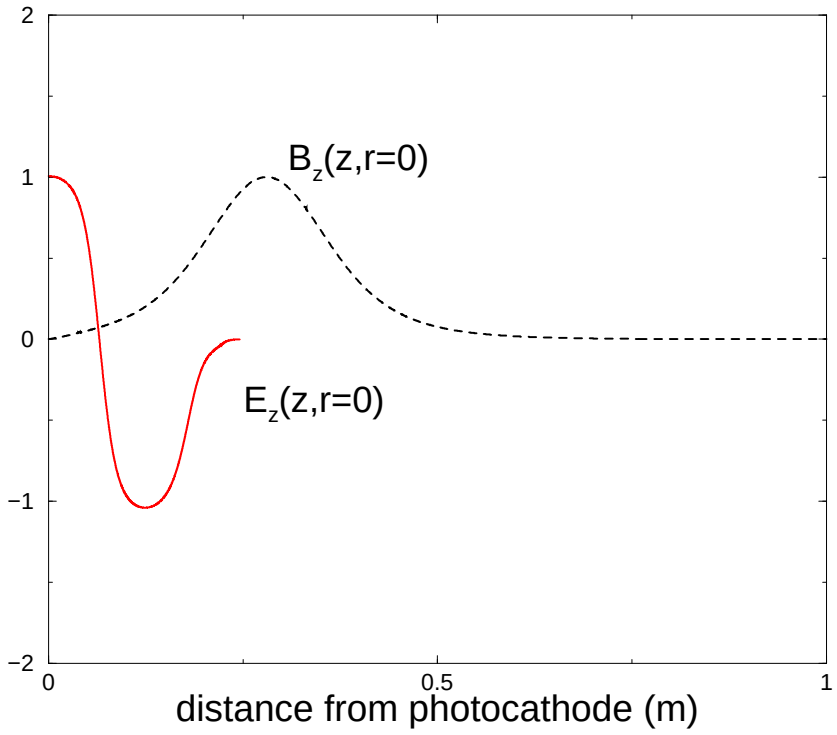


Fig. 4. *On-axis profile of the RF-cavity E-field and the solenoids B-field.*

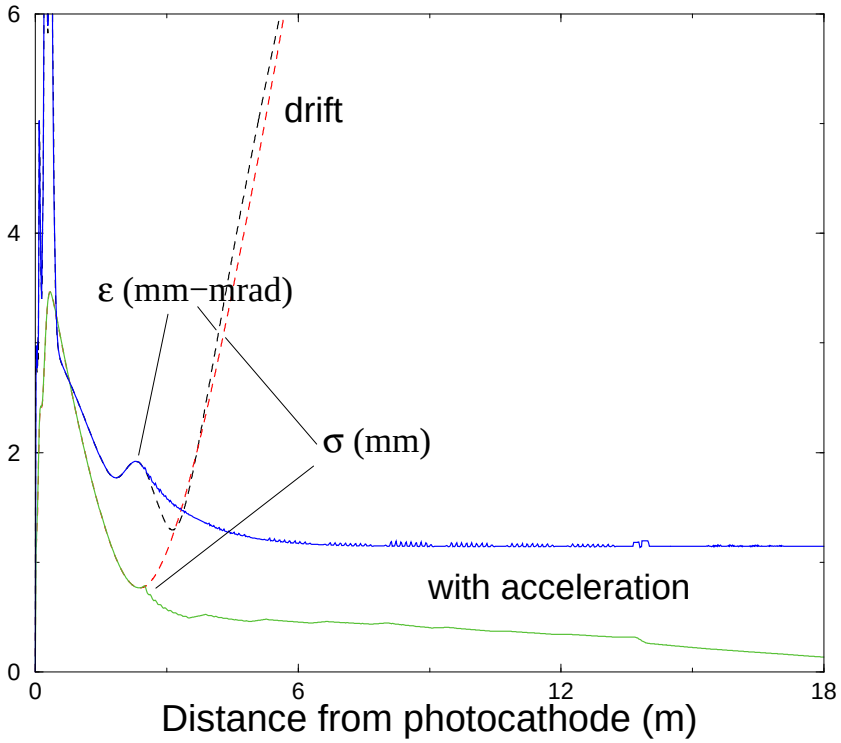


Fig. 5. *Normalized emittance and beam envelope evolutions througout the injector.*

3 Bunch Compression and longitudinal beam dynamics

3.1 Introduction

As mentioned in the previous section, achieving a low transverse emittance requires to start with a rather elongated (FWHM $\sim$ 20 ps) laser pulse on the photocathode. This, in turn, induces an rms bunch length of 2.2 mm, about a factor $\sim$40 larger than that required at the undulator. The bunch is compressed using magnetic compression. Such a scheme consists of an accelerating section followed by an arrangement of bending dipoles. The RF-section is used to introduce a correlated energy chirp along the bunch. Given the incoming longitudinal coordinate of an electron within the bunch (s_o, δ_o) and the RF accelerating voltage V_{RF} and phase φ_{RF}, the induced relative momentum offset δ_i at the exit of the RF-structure is:

$$\delta_i = \frac{\delta_o E_o + V_{RF}\left(\cos(ks+\varphi_{RF}) - \cos(\varphi)\right)}{E_o + V_{RF}\cos(\varphi_{RF})}, \tag{1}$$

where E_o is the injection energy in the accelerating section and k is the RF-wavenumber.

The system of bends, typically arranged as a chicane, introduces an energy-dependent path length variation in such a way that an incoming electron of coordinate (s_i, δ_i) at the chicane entrance is mapped to s_f at the chicane exit as follows:

$$s_f = s_i + R_{56}\delta_i + \mathcal{O}(\delta_i^2). \tag{2}$$

Using this first order formalism and writing $\delta_i = \alpha_1 s_i + \mathcal{O}(\delta_i^2)$, we get the rms bunch length and energy spread:

$$\begin{aligned} &\langle s_f^2\rangle^{1/2} = \sqrt{(1+\alpha_1 R_{56})^2\langle s_i^2\rangle + R_{56}^2\langle\delta_o^2\rangle} \text{ and,} \\ &\langle \delta_f^2\rangle^{1/2} = \langle\delta_i^2\rangle = \sqrt{\alpha_1^2\langle s_o^2\rangle + \langle\delta_o^2\rangle}. \end{aligned} \tag{3}$$

However, there are regimes where the approximation $\delta_i \sim \alpha_1 s_i$ is not verified, for instance when the bunch length upstream of the accelerating section does not satisfy $\langle s_i^2\rangle^{1/2} \ll 1/k$. In such a case the longitudinal phase space accumulates some curvature due to the cos-like dependence of the RF field and one has to write $\delta_i = \alpha_1 s_i + \alpha_2 s_i^2 + \mathcal{O}(s_i^3)$, and take into account the quadratic energy-dependence of the path length in the chicane by introducing $T_{566} = 1/2\partial^2\delta/\partial s^2$. An electron of initial coordinate (s_i,δ_i) is now mapped accordingly to:

$$s_f = s_i(1+\alpha_1 R_{56}) + s_i^2(R_{56}\alpha_2 + T_{566}\alpha_1^2) + \mathcal{O}(s_i^2). \tag{4}$$

In the latter equation one sees that the minimum bunch length is limited by the second order effect in s_i. This limitation points out that the bunch should be compressed at low energy ideally before it accumulated too much RF-curvature. On the other hand compressing the bunch at too low energy might render the space charge force and its associated beam degradation significant (space charge forces scale as $1/\gamma^2$).

To negotiate both effects while compressing the bunch down to the proper bunch length (i.e. to achieve a peak current of 2.5 kA), TTF-2 incorporates a two stage magnetic compression scheme (see fig. 6) and a third harmonic ($f = 3.9$ GHz) RF-accelerating section to compensate for the RF-induced curvature.

Downstream of the 3.9 GHz accelerating section (of accelerating voltage and phase V_{RF39} and φ_{RF39}) the relative momentum offset of an electron is:

$$\begin{aligned}\delta_i = & \frac{1}{E_o + V_{RF}\cos(\varphi_{RF}) + V_{RF39}\cos(\varphi_{RF39})} \times \{\delta_o E_o \\ & + V_{RF}(\cos(ks + \varphi_{RF}) - \cos(\varphi_{RF})) \\ & + V_{RF39}(\cos(ks + \varphi_{RF39}) - \cos(\varphi_{RF39}))\}.\end{aligned} \tag{5}$$

In the latter equation we have enough parameters to (ideally) simultaneously cancel the linear and nonlinear quantities in Eq. (4).

The first magnetic compressor is located at approximately 130 MeV, in the injector area. It reduces the bunch length from 2.2 to ~ 0.4 mm. The chicane is similar to the 4-bend chicane designed for TTF-1 [9] except for a slightly reduced bending angle ($15^\circ < \theta < 21^\circ$). Such a chicane has the feature to be achromatic to all orders in $\delta p/p$.

The second stage compression occurs downstream of the third accelerating module at 440 MeV. The chicane chosen is a S-type chicane [10] optimized to have a minimum emittance dilution due to coherent synchrotron radiation. Its bending angle can be varied ($1.5^\circ < \theta < 5.4^\circ$), but the dispersion is not perfectly closed to all orders.

Linacs:			
parameters	ACC1	ACC2-3	ACC4-5-6
Grad (Mv/m)	12.5/20(4 last cav.)	20	20
RF phase (°)	-9.80	-30.0	0.0
input E (GeV)	0.005	0.13	0.44
final E (GeV)	0.13	0.44	0.95
final $\delta p/p$ (%)	0.93	0.55	0.22
σ_z (μm)	2200	300	50
Compressors:			
parameters	BC2	BC3	
type	standard	S-chic	
Angles (°)	18	3.8	
R_{56} (mm)	-181	-49	
T_{566} (mm)	295	75	
E (GeV)	0.13	0.44	
final $\hat{I}$ (A)	320	2500	

Table 2
Linac and bunch compressor parameters for the nominal operating point.

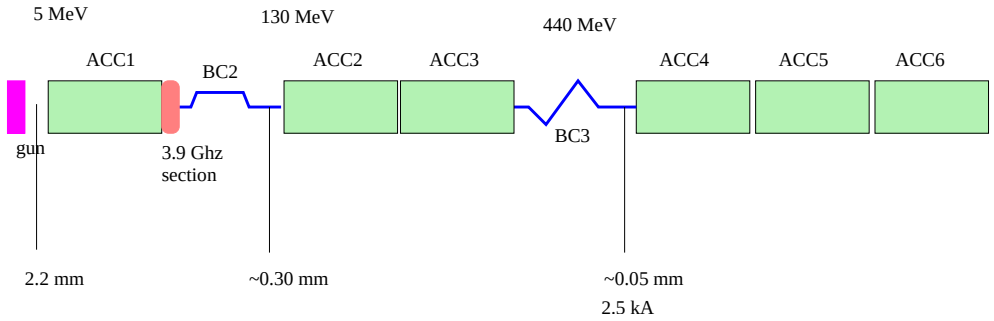


Fig. 6. *Overview of the compression scheme in TTF-2.*

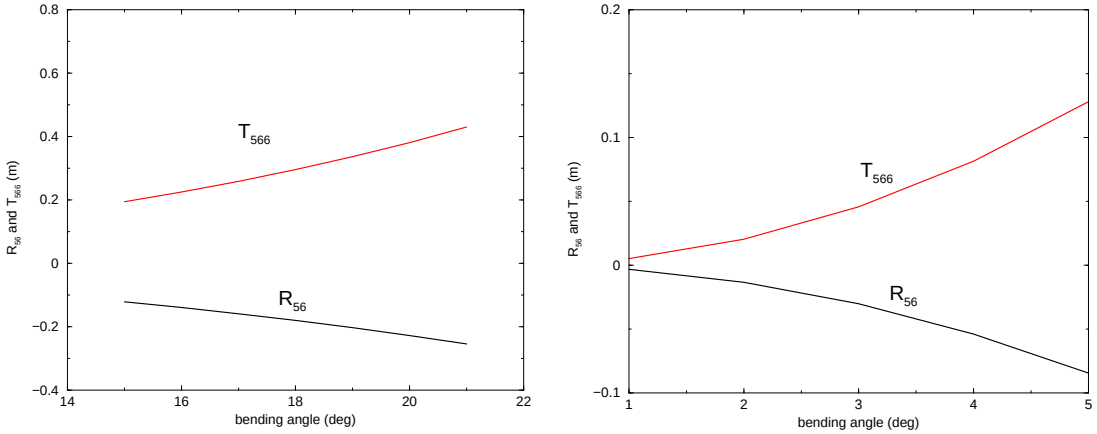


Fig. 7. *linear (R_{56}) and quadratic (T_{566}) momentum compaction of the first (left, BC2) and second (right, BC3) bunch compressors.*

3.2 Results from a 1-d model of longitudinal dynamics

One dimensional simulations of the longitudinal beam dynamics were performed using both a simple analytic model and the single-particle dynamic code Elegant [12]. Here we present the results of the tracking in Elegant. The initial distribution was obtained from Astra [11] and its transverse emittances were enforced to zero. We took into account the geometric wake-field due to the cavities using the steady-state Green function derived in Reference [14].
We identify three modes of operation for the FEL (coming from the incremental upgrade of the compression scheme):

(1) The nominal mode which will be provided once the 3.9 GHz RF-section has been installed,
(2) the femtosecond mode which consists of operating only the first compressor, this will be the default mode of operation for first lasing, and
(3) the intermediate mode where velocity bunching inside the first cavity of ACC1 (see analysis in Ref [15]) will be performed in order to achieve shorter a bunch length upstream of BC2 (to the detriment of transverse emittance).

Of the three aforementioned modes of operation, the first two are presented in figures 8 and 9. The third mode allows to have some tuning over the femtosecond mode (e.g. to render the spike larger) by using the first cavity of module ACC1 as a buncher. However in this latter case there is still a limitation to very high peak current because of the nonlinearities in the longitudinal phase space. The nominal mode is set-up to provide the required peak current of

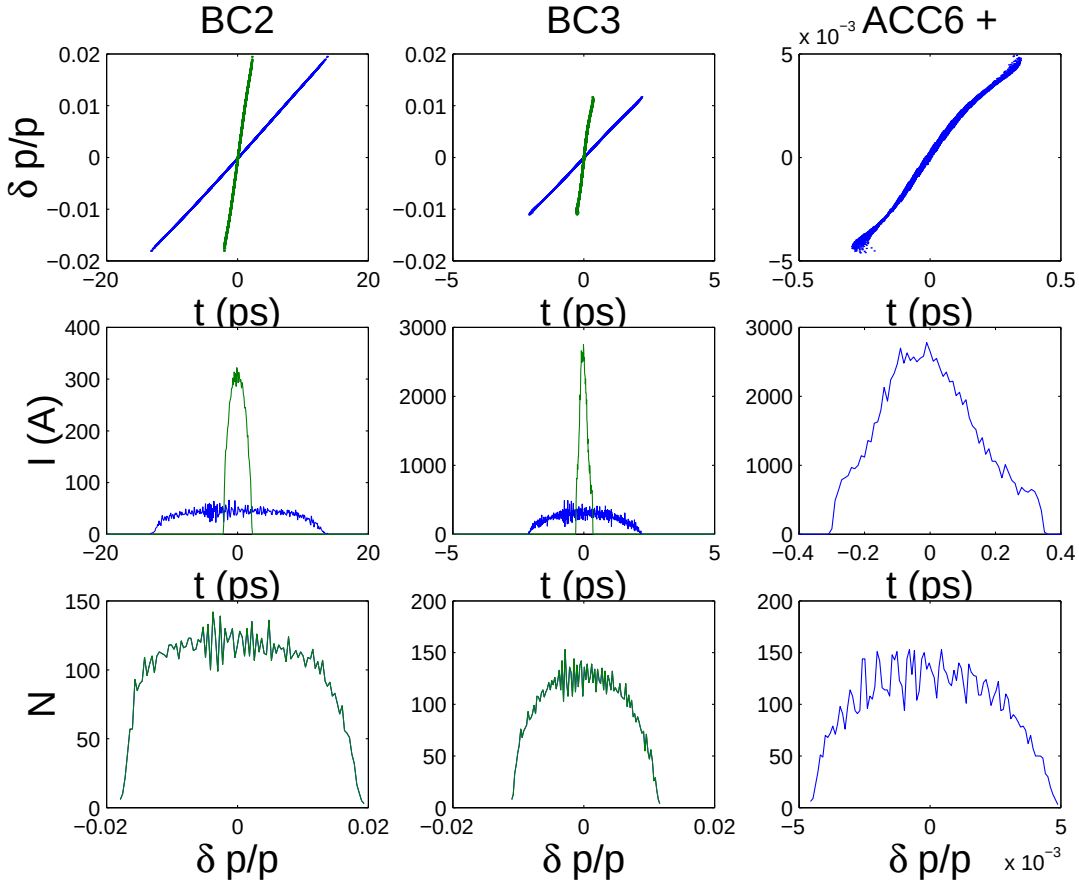


Fig. 8. *Evolution of the longitudinal phase space, peak current, and energy profile for the nominal mode of operation. (blue and green corresponds respectively to before and after the compressor)*

~ 2.5 kA. However there is room to increase the peak current to much larger values (> 5 kA) according to simulation.

3.3 Challenges in bunch compression and transport of the short bunch

3.3.1 Coherent synchrotron radiation

When electrons travel on a curved trajectory, e.g. in bending magnets, they emit synchrotron radiation. Radiation emitted at a retarded time can overtake the bunch on a straight line and interact with electrons ahead in the bunch. This type of bunch "self-interaction" is relevant when the path length in the bend is comparable to the so-called overtaking length defined as $(24\sigma_s\rho^2)^{1/3}$, where σ_s is the rms bunch length and ρ the bending radius. This is the regime of coherent synchrotron radiation (CSR) – the power radiated is $\propto N^2$ (N being the number of electrons in the bunch)[16,17]. This effect is favored in magnetic bunch compressors employed in FEL's and linear colliders, where short (ps-level) and highly charged ($Q \simeq 1$ nC) bunches travel through magnets with small bending radii ($\rho \sim 1$ m). The CSR longitudinal wake function scales as:

$$\widehat{W}_{||} = \frac{Q}{\epsilon_0(2\pi)^{3/2}(3\sigma_s^4\rho^2)^{1/3}}, \tag{6}$$

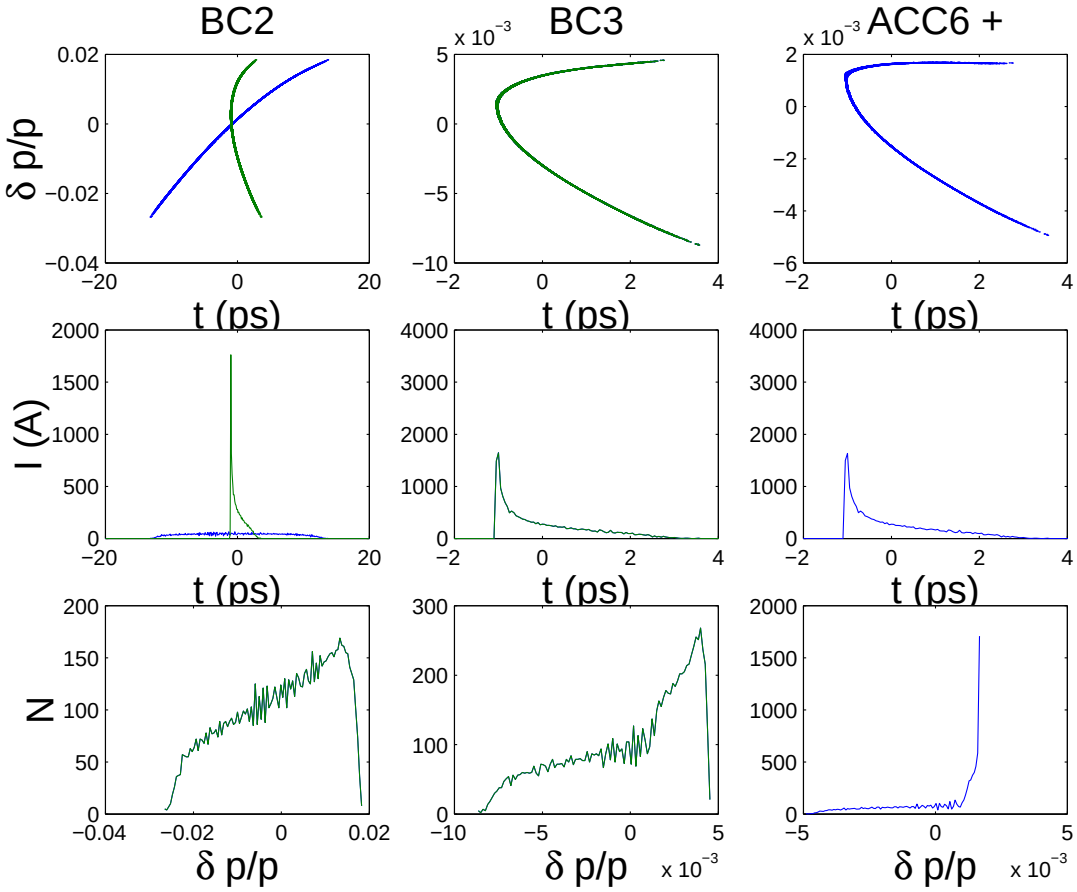


Fig. 9. *Evolution of the longitudinal phase space, peak current, and energy profile for the femtosecond mode. For this mode the BC3 compressor is turned off since BC2 is operated for maximum compression. (blue and green corresponds respectively to before and after the compressor)*

ϵ_0 being the electric permittivity for vacuum. The latter equation assumes the bunch has a Gaussian charge density. In the case of the bending radii and bunch length of TTF-2, the amplitude of the wake function is of the order of 1 MeV. We report on simulation results including this effect in section 3.4

3.3.2 Wake-fields

The principal sources of wake-fields in the TTF-2 accelerator are of geometric and resistive nature. The origin of the first source is discontinuity in the boundary conditions surrounding the beam (i.e. vacuum pipe steps, accelerating cavity, roughness of the beam pipe surface, etc...). The resistive wake-fields come from the finite resistivity of the vacuum pipe. The principal effect (assuming a well centered and short beam) of the wake-field comes from the induced longitudinal monopole mode which induces energy spread. To minimize the effect of resistive wake, the vacuum chamber , starting downtream of the second bunch compressor, will be copper-coated.

3.4 Self-consistent simulation of the compression scheme

The two bunch compressors have been subject to extensive numerical simulations using the computer code TraFiC4 [13].

In the first bunch compressor (named BC2 for historical reasons), we found that the CSR-effect could be strongly reduced by reducing the vertical size of the vacuum chamber to cut off low frequency components of the radiated field. Using an 8 mm gap chamber we found the correlated emittance growth through BC2 is 0.5 mm-mrad while the slice emittance increases by 10%. For the second bunch compressor (BC3) the correlated emittance growth is 0.3 mm-mrad and the slice emittance at the compressor end is about 1 mm-mrad (this is a safe side value since we overestimated the slice emittance downstream of the injector to 0.7 mm-mrad). The projected transverse emittance after the compression process is finalized is expected to be of the order of 1.6 mm-mrad.

4 Beam dynamics in the linac

In the previous sections we have essentially discussed the longitudinal phase space manipulation in the injector and linac. We now concentrate on the transverse dynamics of the linac.

In section 2 we have reported a transverse emittance of 1.2 mm-mrad downstream of the third harmonic accelerating section. There are many factors that can dilute this emittance. Above all, the self-interaction of the bunch via CSR seems to be the most deleterious and requires some attention. The optical lattice functions reflect this: in each compressor we have minimized the beta function in the bending plane at the location where the CSR-induced effects are expected to be largest. In the bending plane, the impact of a CSR-induced angular kick $\langle \delta x'^2 \rangle^{1/2}$ results in an emittance growth:

$$\Delta\tilde{\varepsilon}_\perp/\tilde{\varepsilon}_{\perp o} \simeq \beta\langle \delta x'^2 \rangle^{1/2}/\tilde{\varepsilon}_{\perp o}$$

where β is the beta-function value at the considered location.
Upstream of BC2, a quadrupole triplet is used to minimize the beta function between the 3rd and 4th bends (see Fig. 10). Upstream of BC3 a doublet serves the same purpose (see top plot in Fig. 11).

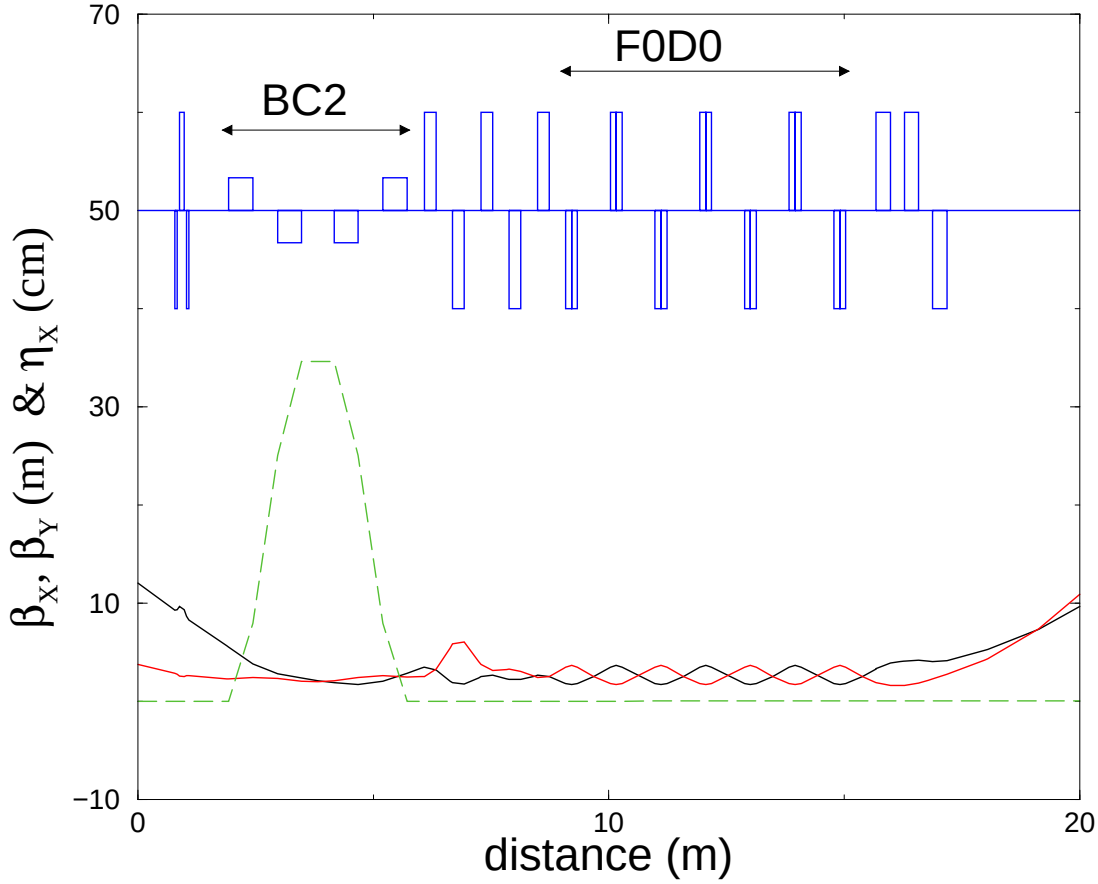


Fig. 10. *Lattice functions in the injector and first bunch compressor BC2 area at 130 MeV beam energy.*

The lattice also incorporates two F0D0 channels with $45°$ betatron phase advance instrumented with a profile monitor to support on-line emittance measurement. Each of these channels is preceeded by a matching section.

The matching into the collimator is done by achieving a round beam in the middle of the first spoiler corresponding to a crossing in the vertical and horizontal betatron function (see bottom plot in Fig. 11).

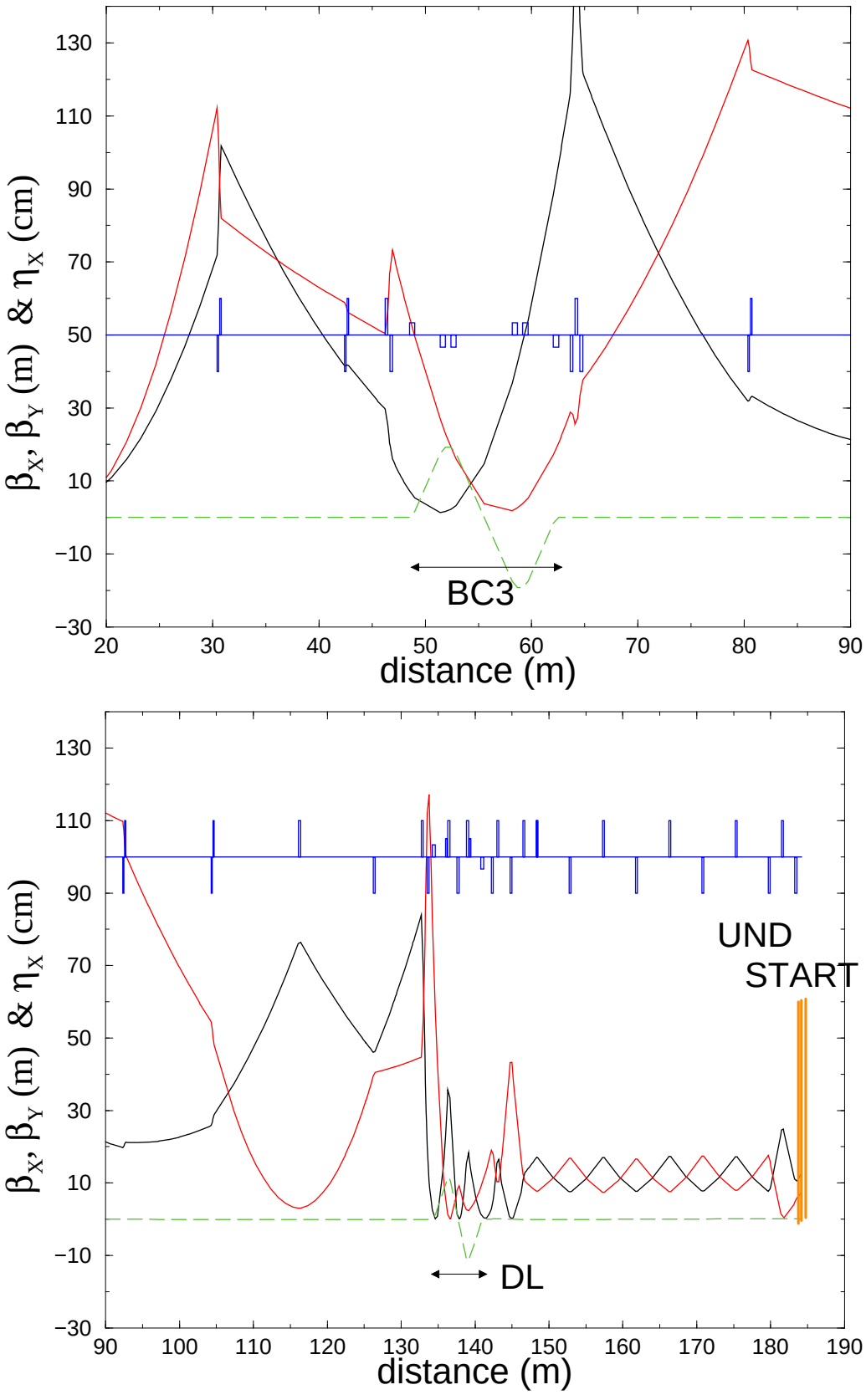


Fig. 11. *Lattice functions in the bunch compressor BC3 (top) area and up to the undulator entrance (bottom) ["DL" indicates the location of the dogleg].*

5 Collimator

Before the electron beam enters the undulator, it passes a long collimation section where particles with wrong energy or momentum are removed from the beam to make sure that they are not lost downstream, damaging the permanent magnets of the undulator. The collimator has been newly designed based on the experience on TTF-1. It collimates five dimensions of the electron beam phase space and takes into account the beam dynamics as well as the interaction of particles with the collimator materials, both in case of an accident and during normal operation at high beam energy and full repetition rate [18]. The collimation section includes four individual collimators, about twenty magnets and electron beam diagnostics. It has the shape of a dogleg, displacing the electron beam axis horizontally by 0.4 m. The principle layout of the system and the mechanical design of the individual collimators are shown in Fig. 12. The water cooled collimator blocks are made from copper with titanium absorber inserts with four different diameters which can be exchanged and adjusted in situ. Only particles with less than 3% energy deviation and with small betatron amplitudes can pass the collimation section and will then go safely through the undulator. Nevertheless, the radiation dose deposited along the undulator will be permanently recorded in order to verify the efficiency of the protection system and to measure the accumulated dose. Since the gap between the undulator magnets and the vacuum chamber is too narrow for conventional online dosimeters, it is planned to install a system based on optical fibers. A prototype optical dosimeter system has been successfully tested on TTF-1 [19,20].

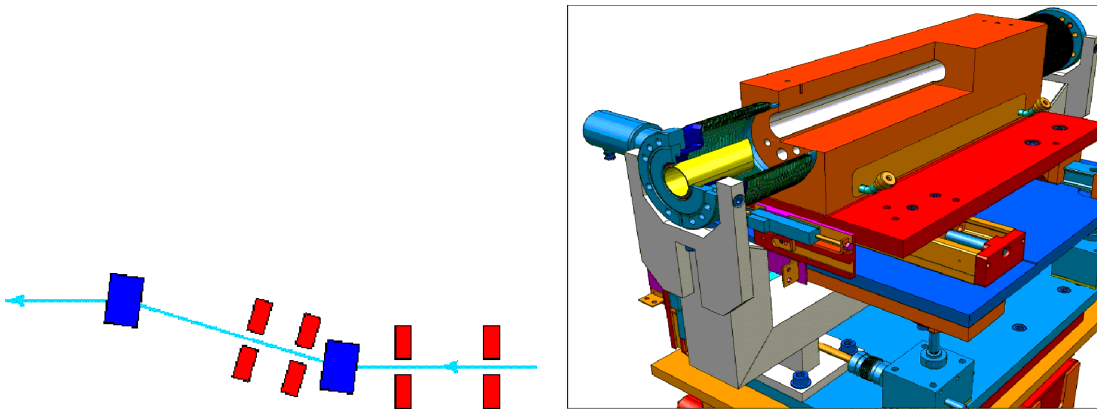


Fig. 12. *Schematic layout of the electron beam collimation system (left) and mechanical design of the collimators (right).*

6 Electron Beam Diagnostics and Intrumentation

The electron beam diagnostics suite includes devices that allow

(1) the measurement of absolute beam and lattice properties, along
(2) with relative measurements that are helpful for monitoring the accelerator stability and setting-up the injector in a reproducible fashion.

6.1 Beam Charge, beam transmission

Downstream of the gun a Faraday cup will provide an absolute charge measurement. Then along the beam-line we will use toroidal AC transformers to measure the charge and monitor beam losses. Four toroids will be located along the injector: (1) upstream and (2) downstream of the booster linac ACC1, (3) downstream of the compressor chicane BC2, and (4) upstream of the second accelerating sections ACC2 and ACC3 (see Fig. 6).

6.2 Transverse phase space

6.2.1 Beam position

The first order moments of the electron beam, i.e. the beam position, must be measured in order to steer the beam on a "golden" orbit, but also to detremine the transverse transfer functions of the lattice. In TTF-2 the beam position will be measured with electromagnetic pickups that consist of antennae in the so-called stripline configuration. This latter configuration minimizes the vacuum chamber discontinuity and thus potential wakefield-induced beam degradation.

6.2.2 Beam transverse density and profiles

The second order moments of the beam, i.e. the beam size, provide indirect information on the beam transverse phase space density. We plan to use electron-to-photon converters and to image the photon source (which mirrors the electron transverse spatial density) using an adequate optical system. At low energy, that is directly downstream of the RF-gun, we will use Yttrium-Aluminum-Garnet (YAG) screens because of their high electron-to-photon conversion efficiency. Downstream of the booster section ACC1 (the first one in Fig. 6), optical transition radiation (OTR) screens will be used; this latter type of screens consists of a thin silicon wafer coated with Aluminum that are inserted in the beam at a 45 deg angle. The backward radiation is then collected by an optical system. For both types of devices, the optical system will consist of a few lenses to vary the magnification along with band-pass filters to decrease chromatic aberration. With proper caution, a resolution of the order of 10 μm can be achieved [21]. In the compressor areas, optical synchrotron radiation (OSR) will be emitted from the bending magnets in the optical regime (the critical wavelengths [1] are $\sim$200 and $\sim$25 nm, respectively, for the first and second compressor) and provides a non-interceptive measurement of the transverse beamspot at dispersive locations.

[1] we use the J.D. Jackson definition for the critical wavelength: $\lambda_{cr} = 2\pi\rho/(3\gamma^3)$, with ρ the bending radius and γ the Lorentz factor.

6.2.3 Transverse emittance

The transverse projected emittance will be measured with two different techniques: (1) the quadrupole scan and (2) the multi-monitor method:

- The former method consists of scanning the gradient of a quadrupole and measuring the corresponding beam size variation downstream. The beam size is a function of the Twiss parameters and emittance, at the quadrupole entrance, and of the transfer matrix between the quadrupole entrance and the observation point. Thus using standard nonlinear fitting techniques and provided the transfer matrix is well characterized, the Twiss parameters and emittance can be computed. The main drawbacks of the method are that (1) it requires some fine tuning of the upstream optics, and (2) many scans may be needed before the measurement converges: the Twiss parameters at the quadrupole entrance (which are at first unknown) should fulfill certain conditions.
- The latter method consists of measuring the beam size at different locations along the beamline. The betatron phase advance between the observation points is crucial: it should be chosen to sample as best as possible one betatron period. That is the reason for the 45 deg phase advance F0D0 cell lattice: four OTR monitors will be installed in this section with a relative phase advance of 45 deg and will therefore sample one half betatron period. Using four monitors separated by 45 deg instead of the mathematically needed three monitors with 60 deg phase advance insure a higher accuracy of the calculated emittance value. Though the multi-monitor method is less precise than the quadrupole scan technique, it provided an almost on-line measurement with no optics tune-up required; it is well suited for regular checking.

The quadrupole scan technique will be implemented at several locations in the machine. Two sections (downstream of BC2, and downstream of ACC6 as shown in Fig. 6) are foreseen to incorporate a F0D0 channel with the proper phase advance to allow on-line emittance measurement using the multi-monitor technique.

Downstream of the gun, the emittance will be verified using the slit-screen technique. Such a method consists of sampling the incoming beam with a slit into a beamlet that drifts up to a YAG screen. The measurement of the beamlet size on the screen provides an estimate of the angular spread.

6.3 Longitudinal phase space

6.3.1 Energy and energy spread

The beam energy and energy spread can be measured at several dispersive loactions: in the gun spectrometer (at 4-6 MeV), in the BC2 and BC3 bunch compressors, in the dogleg serving for energy collimation and in front of the beamdump downstream of the undulator.

To quantify the compression process we plan to measure the longitudinal transfer maps $\partial s_{in}/\partial s_{out}$ between the photocathode and the bunch compressor exit. This technique [22,23] provides (1) a way of setting up the machine in a very reproducible manner along with (2) quantitative information on the lattice map Taylor expansion (i.e. R_{55}, T_{555}). The hardware consists of a pickup cavity that measures the relative time-of-flight of the electron bunches while the photocathode drive laser phase with respect to the master oscillator is varied. Simulations have shown that the technique, for instance, is sensitive to phase variation of the booster linac

and third order harmonic section at the 1 deg level. A similar technique, but this time varying the gradient of a cavity and measuring the relative time-of-flight, can provide the same kind of diagnostics for the $\partial\delta_{in}/\partial s_{out}$ map which in turn gives quantitative informations on the coefficients R_{56} and T_{566} (and higher order) i.e. the linear and quadratic momentum compaction.

6.3.2 Bunch length

Time domain techniques: Downstream of BC2, and for nominal operation of this compressor ($\sigma_z \sim 300 - 500\ \mu m$), the bunch length will be measured with a 200 fs resolution Hamamatsu streak camera currently in operation at TTF-1. The camera will be used to streak either OTR or OSR emitted in the BC2 area.

In the straight section downstream of ACC6, we plan to use an S-band deflecting mode (TM_{11}) RF-cavity provided by SLAC. Such a deflecting cavity will be used to introduce a longitudinally-dependent transverse kick along the bunch. Thus different longitudinal slice will have different orbit and a viewer located downstream of this cavity will provide the same information as a standard streak camera does. On another hand, if the screen is located in a dispersive section downstream of the deflecting cavity, it will provide a complete picture of the longitudinal phase space (see Reference [24]).

The bunch length remains constant within the booster linac and up to the compressor entrance. Within the linac (ACC4,5,6) it can be measured using the zero-phasing technique: the last cavity of the linac is operated at zero-crossing to introduce a linear correlation between δ and s. The energy spread profile, measured in a downstream dispersive section, directly relates to the longitudinal bunch profile and can thereby provide information on the bunch length and longitudinal phase space slope before the "zero-phasing" cavity entrance [25].

Frequency domain techniques: Downstream of the compressors, we plan to use synchrotron and/or transition radiation emitted in the coherent regime, i.e. at wavelengths $\lambda > \sigma_s$. The spectrum of such radiation can directly provide information on the bunch form factor (BFF) (i.e. $|\mathcal{F}[S(t)](\omega)|^2$, $S(t)$ being the charge density and $\mathcal{F}$ stands for the Fourier transform) [16]. The technique gives some hints on the bunch length and with some assumption one can retrieve the charge density using the dispersion relation to reconstruct the (lost) information on the complex part [26] of the radiated field. The method can also serve as a bunch length monitor (relative measurement) and/or, by observing simultaneously several frequency components of the BFF, as a monitor of RF-subsystem stability in the injector (e.g. phase/gradient of booster linac).

7 Undulator system

7.1 Introduction

Phase-2 is planned to be an extension of Phase-1 to shorter wavelengths as low as 6 nm [30]. This possible extension was kept in mind already from the very beginning of Phase-1. Expensive hardware components such as undulator magnet structures were designed to be used in Phase-2 as well. A radiation wavelength of about 6 nm can be obtained by raising the electron energy to 1 GeV. In order to reach saturation the magnetic length of the undulator system has to be doubled, i.e. six instead of three undulator segments as was the case for Phase-1 will be needed. The total length will be almost 30 m. At a later stage, after commissioning and use of the FEL in SASE mode, the FEL will be extended by further undulator segments and other components in order to realize a seeding scheme to produce fully coherent radiation for user experiments [31].

Table 3
Comparison of parameters of the undulator systems of Phase-1 and Phase-2

		TTF-1	TTF-2
Undulator Period Length	mm	27.3	27.3
Gap	mm	12	12
Peak field	T	0.47	0.47
K-Parameter		1.17	1.17
Electron beam energy	GeV	0.23	1.0
Segment length	m	4.4922	4.4922
Distance between Segments	mm	325	710
Focusing Type		integrated, FODO	separated, Doublet
Quadrupole type		Permanent magnet	Electro-magnet
Quadrupole distance	mm	477.75	5000 / 400
Quadrupole gradient	T/m	17	37
Quadrupole length	mm	163.8	82
Average β function	m	1	4.0
bMax / bMin	m	3.0	3.0
Saturation length	m	12	27

7.2 Modifications on the Undulator System

The undulator system for Phase-1 was optimized without compromising on FEL performance and saturation length [32–35]. The result was a magnet structure with an integrated combined strong focusing FODO lattice consisting of 15 focusing and 15 defocusing quadrupoles. It allowed for an optimum average β function inside the undulator of only 1m at a beam energy of 0.3 GeV. For Phase II at 1 GeV $\beta \approx$ 3m would be possible. By choosing a small quadrupole distance the influence of β-variations on the FEL process was kept negligibly small. Such a combined function undulator is much more difficult to design, build and tune than a conventional one. In addition for high accuracy electron beam orbit control one corrector and one Beam Position Monitor (BPM) per quadupole is required. They have to be integrated into the vacuum chamber inside the undulator gap, which therefore needs a quite sophisticated design

[36,37]. Based on the good and successful experience made in Phase-1 the requirements on undulator performance, average β function, β function beat, numbers of correctors and BPMs were revised [38]. A separated focusing system was investigated, in which the boundary conditions set by the already existing hardware were carefully considered. Full advantage will be taken from the modular magnet design used for Phase I. The focusing magnets, which can be considered as additional attachments to a hybrid type magnet structure will be omitted. Thus period length, gap and total lengths of the magnet structures are kept unchanged and only the plain, conventional Halbach Type Hybrid Structure will be used further. The focusing will have to be accomplished by quadrupole doublets placed in between two neighboring undulator segments. Consequently the vacuum chamber design can be considerably simplified as compared to Phase-1. The quadrupoles of the doublets need to have a distance of 510 mm. This gives plenty of space for diagnostic equipment. These components are described below. Table 3 shows a comparison between the two alternatives. Although a combined focusing solution offers the shortest overall system length there is much more effort needed for magnetic measurements, fine tuning magnetic as well as mechanical alignment, vacuum chambers, beam position monitors and correctors. Therefore the setup of the undulator system is considerably simplified on going to separated focusing. There are drawbacks, which have to be mentioned: First, additional length is required for the quadrupoles in the intersections and to compensate for the debunching in the quadrupole doublets. Second, the resulting average β-function is somewhat larger than its optimum value. These issues have been worked out in detail in Ref [38]. A comparison of key device parameters of Phase-1 using the combined focusing and Phase-2 with the separated solution is shown in Table 4.

7.3 Intersections

Figure 13 shows the focusing/diagnostics unit which will be placed before, between and at the end of the undulator modules . The vacuum pipe crosses two quadrupoles and will be connected with the the undulator vacuum chamber on both sides. The two quadrupoles are supported by a two axis drive system, which will allow to position the quadrupole axis in the horizontal and vertical direction with a relative precision better than 5 μm. In the centre of the whole device a diagnostics block is installed which carries a cross of pick up BPMs of the type used already in the undulator vacuum chamber during TTF phase-1. Additionally two wire scanners for horizontal resp. vertical scans of the electron beam are attached to the block. To reduce the size and the weight of the whole set up, a new scanner type was developed. Figure 14 shows a photograph of the first prototype. First tests of the mechanics were done successfully at DESY - Zeuthen. The fork with the wires (to be seen on the left side of the figure) is driven by a special reverse spindle drive powered by a stepping motor. The maximum anticipated scanning speed of 1m/s was achieved. In the slow speed operation mode a linear resolution better than 5 μm will be possible. To fulfil the high demands on position stability and precision all components are mounted on a granite bench which is supported by a concrete block. It is planned to install a wire system to control the long term stability of all 7 devices relative to each other.

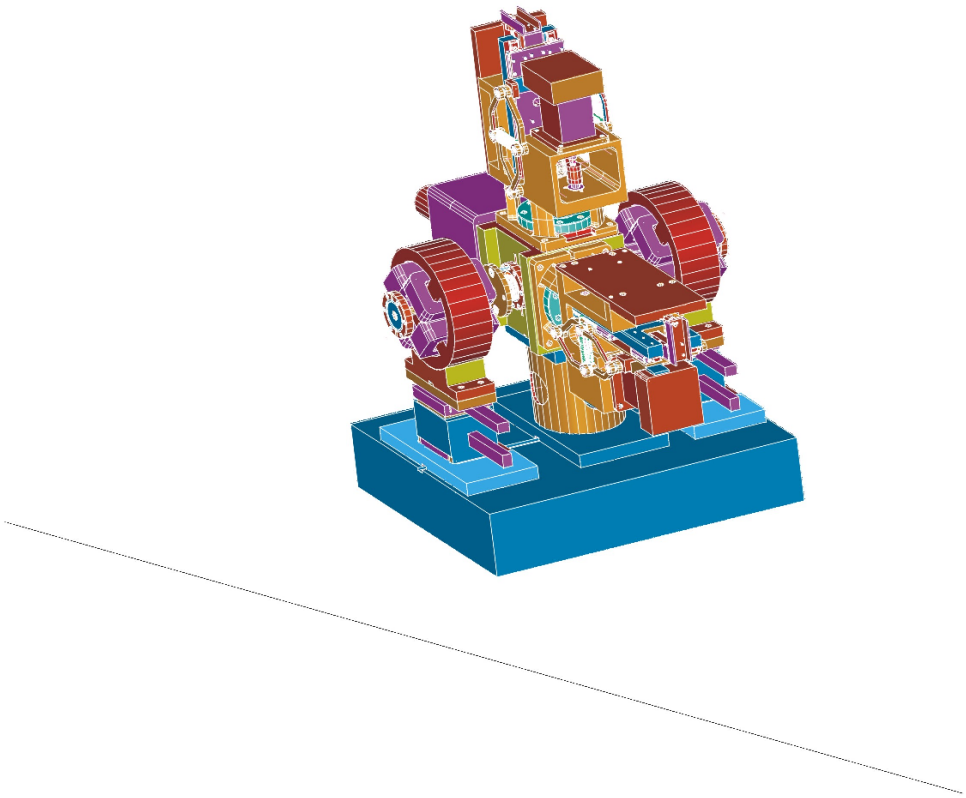


Fig. 13. *The diagnostic and beam optic station between the undulators*

7.3.1 Vacuum Chambers

The new set up simplifies the vacuum chambers. We will use the proven vacuum chamber design using extruded aluminium profiles developed at the APS [37]. The number of monitors in the undulator gap region will be reduced to two. Three steering coils of reduced strength will be installed in the center of each undulator. The manufacturing of the chambers is planned for 2002 at our collaboration partners at the APS in Chicago.

7.3.2 Quadrupole alignment

One of the most important issues in an FEL is the transverse overlap of electron and photon beam. One main reason for beam misalignment is misalignment of quadrupoles. It is one of the great advantages of the separated focusing structure chosen for Phase-2 to have electromagnetic quadrupoles. Their strength can be chosen independent of the electron beam energy. This will allow for better, faster and more efficient beam based alignment techniques. For permanent magnet quadrupoles as used in Phase-1 the only means of checking quadrupole offsets is the variation of the electron beam energy, which requires very stable operating conditions. Appropriate alignment procedures have been proposed [39,40]. The advantage of the separated focusing is that on one hand less focusing elements are needed, resulting in less kicks of the electron beam. On the other hand, the alignment procedure can now be performed by varying the quadrupole strength instead of changing the beam energy. Thus, the initial conditions do not have to be changed at all.

The alignment procedure proposed to align the electron beam varies the quadrupole exci-

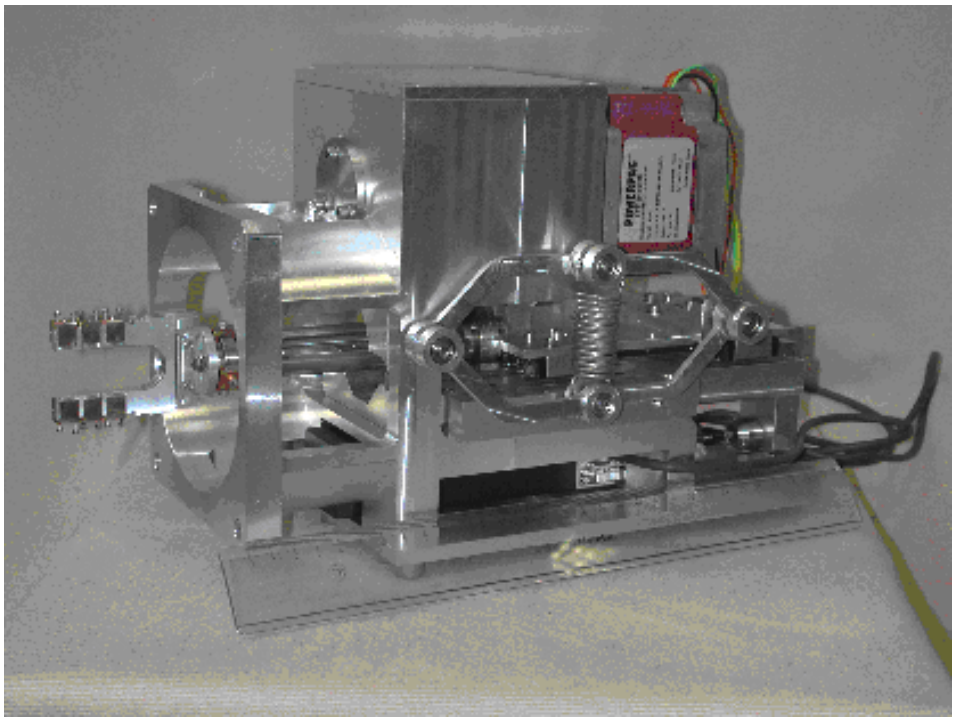


Fig. 14. *The new wirescanner module.*

tation by 20% around its nominal value. The orbit displacement measured at a downstream beam position monitor is used as indication for the displacement of this quadrupole. If the beam doesn't move, the beam is going straight through the quadrupole center. If it moves, the quadrupole offset can be calculated from the measured displacement. The procedure has to be repeated for each quadrupole to be adjusted. In Fig. 15 the potential of the proposed beam based alignment procedure is demonstrated: In the top figure the probability distribution of the RMS electron beam orbit is shown. 1000 different electron orbits through the undulator system were calculated. In these simulations the quadrupoles were randomly displaced by $\pm 200\,\mu$m. Depending on a specific error configuration the RMS values extend above 600 μm. Its average RMS is 206 μm. The bottom figure shows the orbit deviation after a single correction of the quadrupoles using the above mentioned beam based alignment procedure. Approximately 90% of the orbits is within the 15 μm, which is the tolerable RMS orbit deviation (20% of the transverse RMS beam size, see Ref. [41]). Large deviations can still be reduced by repeating this procedure several times. The ultimate accuracy is determined by the resolution of the BPMs which was assumed to be 5μm. Errors in the undulator structures have not been taken into account in this alignment procedure. Experience has shown, however, that these errors can be neglected in practice [42,43].

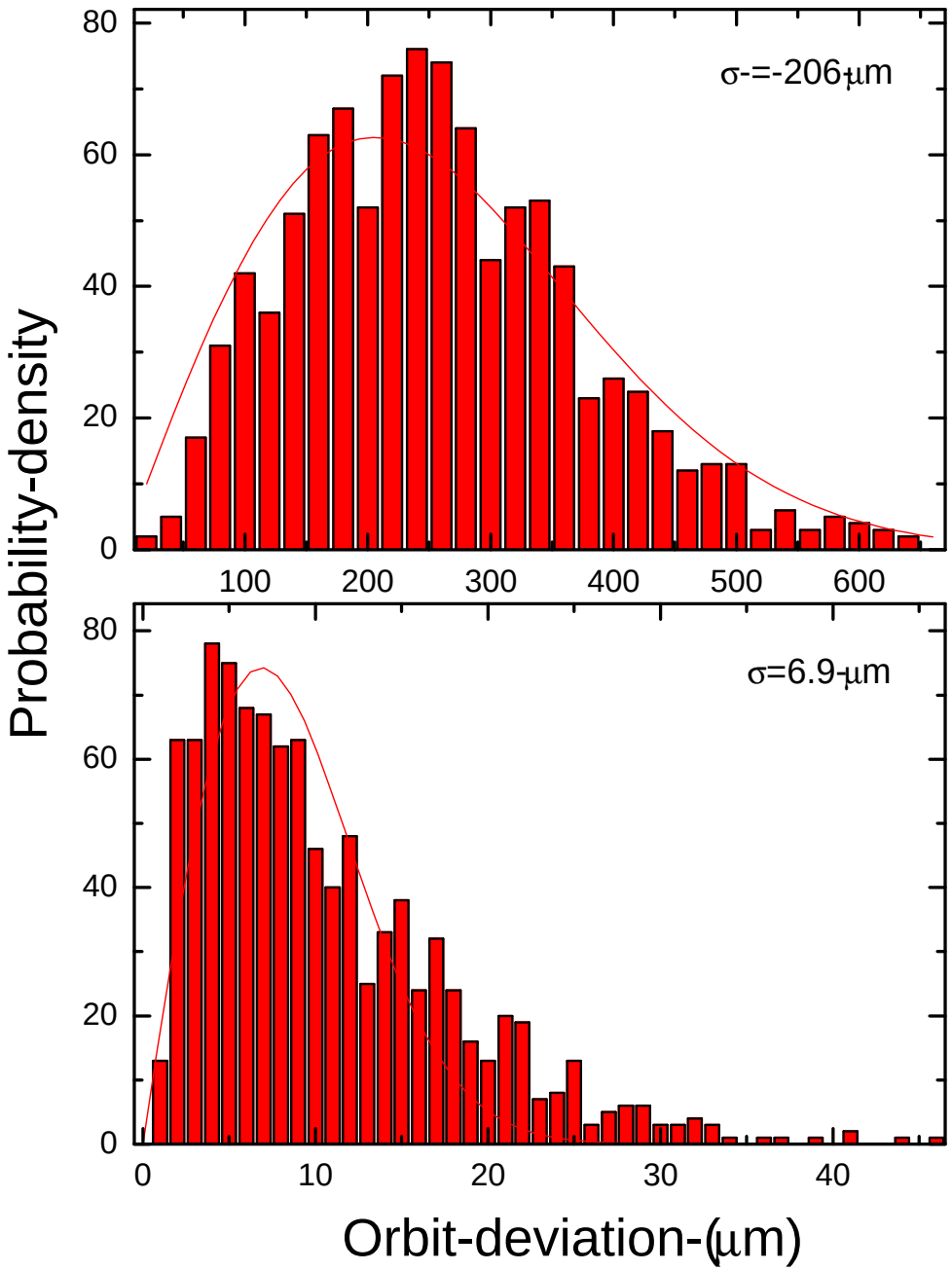


Fig. 15. *Probability that the orbit deviates from the ideal one before (top) and after (bottom) beam based alignment. The assumed resolution of the beam position monitors is 5 μm. Initial beam jitter is not taken into account.*

8 Photon beam distribution and user facility

Design and construction has started for the FEL user facility including the radiation transport to the experimental area, the distribution of experimental stations in the FEL hall, a monochromator for experiments at high energy resolution, a pump-probe facility for time resolved studies, photon beam diagnostics, and a seeding addition. The most important input for the technical design are the photon beam parameters which are discussed in section 9. In particular the photon beam propagation has changed due to the change of the electron beam focusing along the undulator. This leads to a different scaling of source size and beam divergence with wavelength compared with the previous design. Tables 4-6 contain the results of numerical simulations for five different wavelengths. For 60 and 120 nm it was assumed that only the first bunch compressor is used.

8.1 Photon beam transport and distribution of experimental stations

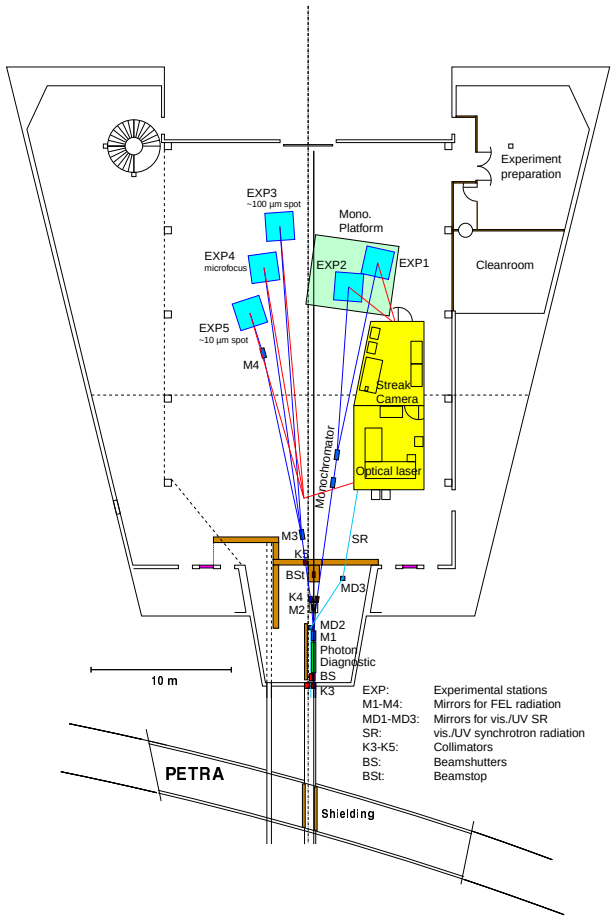


Fig. 16. *Preliminary layout of the FEL beam transport and the experimental area*

The FEL photon beam has to be transported from the last bending magnet in front of the electron beam dump over a distance of about 30 m into the experimental hall. On its way it crosses the PETRA tunnel approximately half a meter below the particle beam (see Fig. 16). 80 cm wide steel tubes have been installed between the TTF and the PETRA tunnels and between

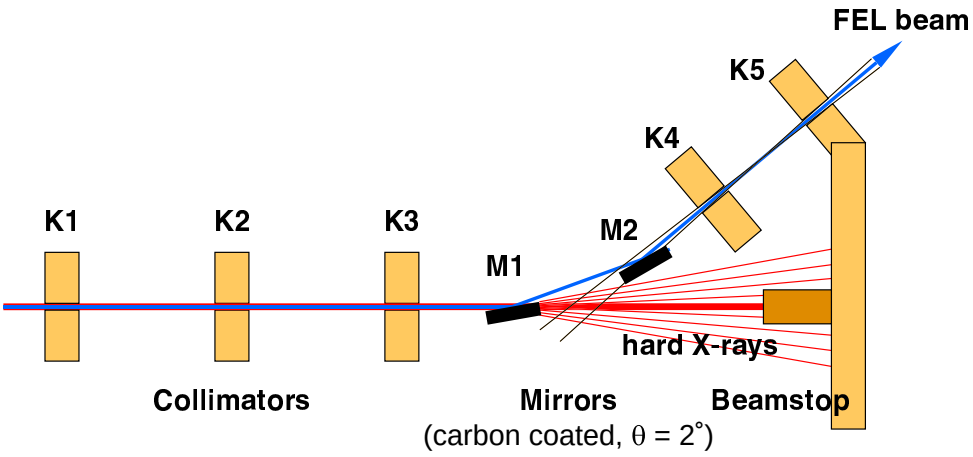


Fig. 17. *Principle of the radiation protection for the experimental area (top view)*

PETRA and the FEL hall in order to leave sufficient space for future developments. The long distance between the radiation source and the FEL hall has two major advantages:

(1) The photon beam can be well collimated facilitating radiation protection of the experimental area and reducing the interference between TTF and PETRA to a minimum.
(2) The photon beam can diverge so much that the power density absorbed by the first optical components is acceptable.

The collimation system consists of five apertures (K1-K5 in Figs. 16 and 17) and will accept a photon beam with 0.5 mrad diameter. Two collimators are located above the electron beam dump at the end of the TTF tunnel in order to reduce the level of gamma radiation leaving the tunnel towards the FEL hall and to prevent this radiation from striking the vacuum tube inside PETRA. Together with radiation shielding around this tube in the PETRA tunnel and two beamshutters (BS), one at the end of the TTF tunnel, and one at the entrance of the FEL hall, it should be possible to make TTF and PETRA operation almost independent. It is also intended to build a new access to PETRA in order to avoid dismounting the FEL beam line in case of PETRA maintenance in the area between TTF and the proton injection line into HERA. The third collimator (K3) at the entrance of the FEL hall defines a narrow beam containing the FEL radiation and a hard X-ray (bremsstrahlung) background. The FEL radiation is then reflected by two mirrors, M1 and M2, before it enters the experimental area through another two collimators, K4 and K5. The latter are designed such that M1 cannot be seen from the experiment to make sure that hard X-rays scattered off M1 do not enter the experimental area. The principle of the radiation protection is shown in Fig. 17.

Typical incidence angles for most mirrors will be 2° in order to reduce the absorbed power density to a tolerable level. The mirrors need to be about 0.5 m long to collect the full radiation beam for the complete spectral range of the FEL. The reflecting surface will be a thin carbon coating on a water-cooled silicon substrate. Carbon has excellent optical properties and is superior to other materials in this spectral range (see Fig. 18). High reflectivity is essential for reducing the risk of damage due to the high FEL peak power and for minimising thermal deformations of the mirrors at high FEL repetition rates.

In order to make effective use of the FEL beam, it can be steered to different experiments just by switching one or two mirrors. While one experiment is online, the others can be prepared

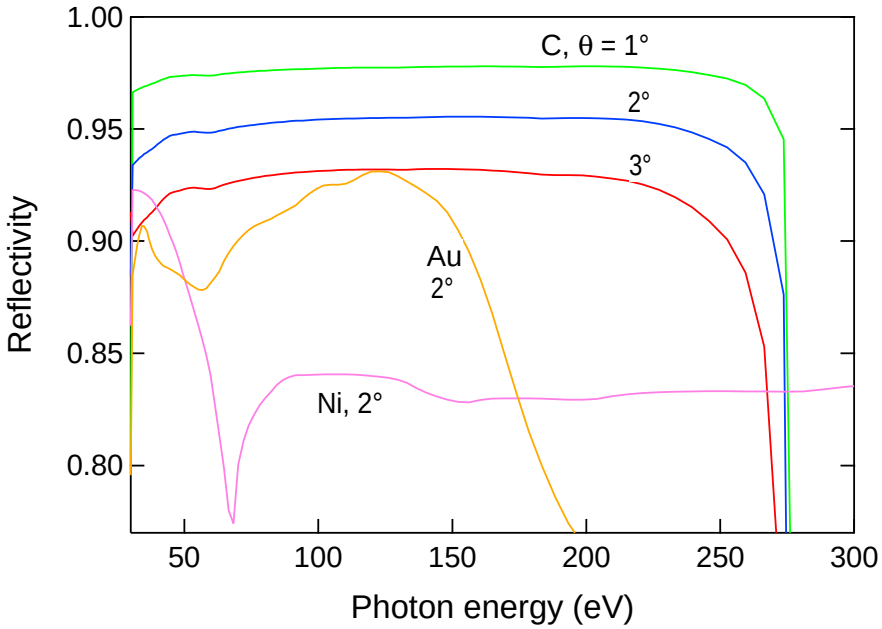


Fig. 18. *Calculated reflectivities of C at* $1°$*,* $2°$ *and* $3°$ *grazing angle of incidence, and Au and Ni at* $2°$

or exchanged. It seems realistic to connect about five experimental stations simultaneously as shown in Fig. 16. Two experiments (EXP1 and EXP2 in Fig. 16) can be served by a high resolution monochromator, the other three use the direct FEL beam. It is planned to install two plane mirrors at the M1 position, pre-aligned at a glancing angle $\theta = \pm 2°$, to steer the beam either to the right into the monochromator, or to the left to one of the other experiments. The M2 mirror will be plane in the left branch and toroidal in the other where it will be part of the monochromator optics. There are three options for the direct beam on the left:

(1) It can go from M2 straight down to the experiment (EXP4), where a special focusing element with short focal distance just in front or in the experimental chamber can produce a sub-μ spot on the sample.
(2) It can be deflected to the right by $4°$ into EXP3 by a focusing mirror M3 imaging the FEL source down to a size of ~ 100 μm.
(3) It can be deflected to the left by a plane mirror M3 and further by a focusing mirror M4 to produce a spot size of ~ 10 μm on a sample at EXP5.

The vacuum system will include fast closing valves as well as differential pumping in each beamline in order to protect the optical components and the other beamlines. Great care will be taken to maintain a clean, particle- and hydrocarbon-free vacuum environment and to prevent the transport of dust particles to the optical components or even into the undulator area.

8.2 Monochromator for high energy resolution

A high resolution monochromator has been designed for experiments which need a photon bandwidth much narrower than the natural width of the FEL source. This project is a collab-

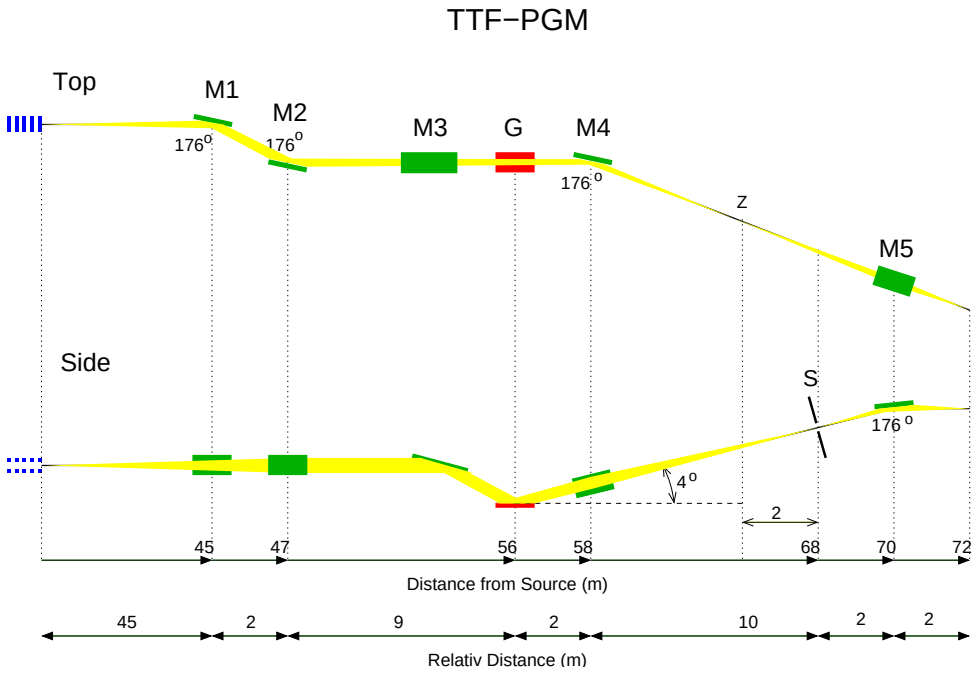


Fig. 19. *Layout of the high resolution plane grating monochromator*

oration between the University of Hamburg, BESSY and HASYLAB with funding from the BMBF. The instrument is based on the standard plane grating monochromator developed at BESSY, combining high energy resolution and high throughput [27]. The layout is shown in Fig 19.

The original design has been slightly modified to reduce the power load on the grating and the pre-mirror M3. The exit arm of the monochromator is rising at an angle of 4° such that the sample position will be approximately 2.5 m above the floor level. The tuning range of the monochromator will include the full FEL spectral range and higher harmonics up to about 1 keV photon energy. The monochromator will also provide the possibility for characterising the FEL photon beam. It is planned to use a phosphor screen in the exit slit plane together with a gated camera to measure the spectral distribution of single FEL pulses. The monochromator should be available with the start of the user facility in 2004.

8.3 Pump-probe facility for time resolved experiments

Another important development for the FEL user facility is a synchronised optical laser system making it possible to exploit the intense soft X-ray pulses from the FEL for time-resolved measurements down to the level of the pulse width, i.e. close to a hundred femtoseconds. The project is a collaboration between HASYLAB, Max-Born Institute, Research Centre Jülich, Dublin City University, MAX-Lab/Lund Laser Centre and CNRS/LURE and is funded by the Fifth Framework Programme of the European Commission. The objectives are the development and test of a flexible, high-power laser system, a precise synchronization with the free electron laser, and a user interface to combine the two photon beams for pump-probe experiments. The system is planned to be available for first test experiments soon after the start of the FEL in 2004.

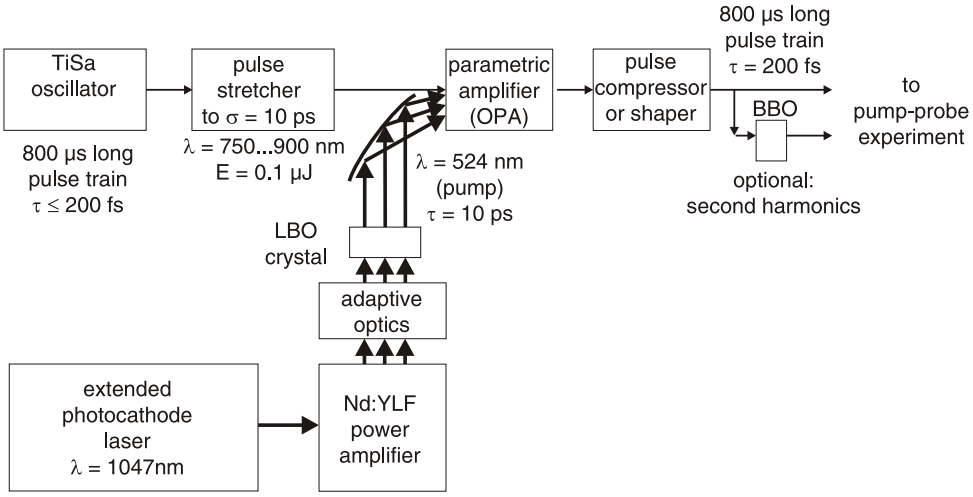


Fig. 20. *Schematic layout of the optical laser system*

The schematic layout of the laser system is shown in Fig. 20. In order to provide sufficient flexibility for the users, the laser must have a wide tuning range, flexible pulse shaping, and the highest possible average power during the FEL pulse train (0.3 - 0.5 kW optical laser power). This requires the development and construction of an optical parametric amplifier (OPA), pumped by a unique, frequency doubled Nd:YLF laser with 10 ps pulse length and up to 5 kW average power during the millisecond pulse train. The pump laser is based on the photocathode laser used for the electron beam injector which has been in operation at TTF-1 for more than two years [28]. Grating combinations will be used to adapt the duration of the seed-pulses from a Ti:sapphire oscillator to the pulse duration of the pump laser and recompress them after parametric amplification (CPA, Chirped-Pulse Amplification).

The synchronisation of the optical laser with the FEL pulses to within 200 fs is extremely difficult, in particular since they are independently locked to the same master oscillator which is also the reference for the accelerator RF system. The electronic synchronisation which includes the feedback loop stabilising the laser cavity, has to be pushed to the technical limits. Slow drifts between the two systems will be corrected by an online phase detector deriving a signal from the electron bunches behind the undulator which are synchronous with the FEL pulses. For this purpose it is planned to extract visible to near UV synchrotron radiation from the last bending magnet and to transport it to the optical laser hutch in the experimental hall (the yellow box in Fig. 16) where it is focused on a fast streak camera together with a part of the optical laser pulse. The synchronisation is schematically shown in Fig. 21. In addition it is necessary to develop a precise, absolute phase measurement. At the moment it is not clear how much uncorrelated time variation of the FEL pulses may be coming from the accelerator due to instabilities in the RF system and related phase shifts in dispersive sections. Such time jitter cannot be corrected by a feedback and would thus limit the achievable level of synchronization. If statistical jitter is significantly larger than the FEL pulse duration, no matter whether it comes from the accelerator or insufficient electronic synchronisation, an online precision phase measurement for each pulse is mandatory for high resolution experiments.

The third part of the project includes the development of a user interface and the commissioning and verification of the complete system on the FEL. In order to make efficient use of such a complex facility it is necessary to develop a user friendly interface which provides in-

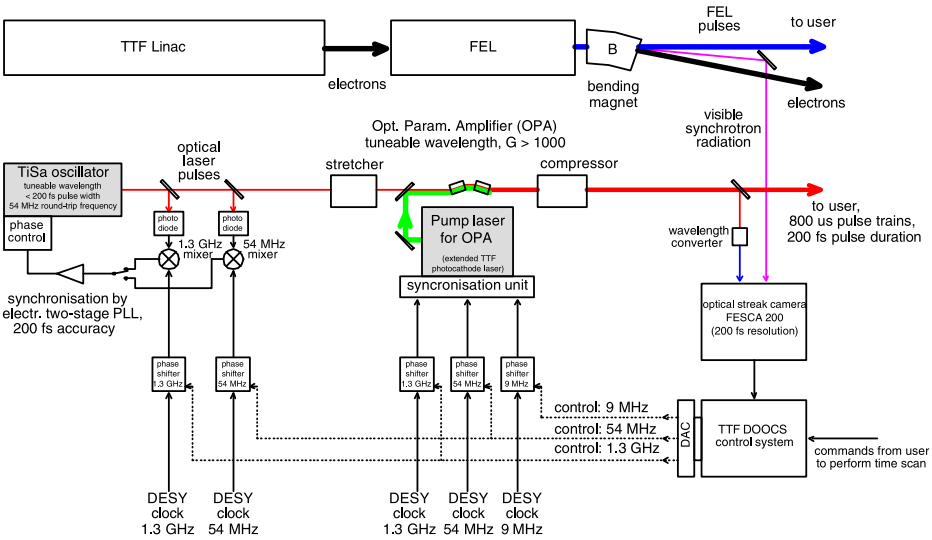


Fig. 21. *Principle of the synchronisation of the optical laser and the FEL*

formation on all important parameters and allows to control them. This requires the permanent integration of online FEL photon beam diagnostics into the facility, the design and construction of hardware components to steer and combine the two photon beams onto a solid or gas-phase sample, and the complete hardware electronic and software integration of all systems including accelerator and FEL.

In general all user end-stations need permanent access to online photon beam diagnostics with single pulse resolution. Much of this diagnostics has to be newly designed to cover the full spectral range.

9 Expected parameters of radiation

TTF FEL at DESY will cover continuously the wavelength range from 120 to 6 nm. Three modes of operation are currently foreseen:

(1) short wavelength mode ($\lambda = 6 - 30$ nm, pulse duration 200 fs);
(2) long wavelength mode ($\lambda = 30 - 120$ nm, pulse duration 1 ps);
(3) femtosecond mode ($\lambda = 30 - 120$ nm, pulse duration 50-100 fs).

Operation of the FEL in the short wavelength mode requires the complete chain of bunch compression scheme, i.e. BC2, BC3, and the 3rd harmonic of the RF section in the injector (see Sec 3). Operating range of the electron energy is from 460 to 1000 MeV, the required peak current is 2500 A. Operation of the FEL in the long wavelength mode requires BC2 and the 3rd harmonic RF section. The operating range of the electron energy is from 230 to 460 MeV at a peak current of 500 A. The longitudinal profiles of the electron bunch for these modes of operation are shown in Fig. 8. The femtosecond mode of operation is based on the experience obtained during operation of TTF-1. This mode of operation requires BC2 only. An electron bunch with a sharp spike in the head of the bunch is prepared with an rms width of about 20 μm and a peak current of about 1 kA (see Fig. 9). This spike in the bunch generates FEL pulses with a duration below one hundred femtoseconds.

9.1 Short and long wavelength mode of operation

Tables 4 and 5 give an overview of the expected FEL parameters. Figure 22 shows the dependence of the saturation length on the operating wavelength. It is seen that the use of six undulator modules will allow to reach saturation in the whole operating wavelength range. The performance of the FEL is critically depending on the value of the emittance. It is seen from Fig. 23 that the saturation length increases dramatically for a normalized emittance of 4π mm-mrad, and saturation can not be reached within six undulator modules. A more extended overview of the FEL properties is given in graphical form. Figures 24 and 25 show the evolution of the energy in the radiation pulse versus undulator length. Plots for the peak and average brilliance are presented in Figs. 26 and 27. Figures 28-45 present the expected time and spectral structure of the radiation pulse, the intensity distribution in the near zone, and the angular distribution in the far zone.

9.2 Femtosecond mode of operation

An overview of the femtosecond mode of operation is given in Table 6. Figure 46 shows the saturation length in this wavelength range. It is seen that the wavelength range 30-120 nm is covered by six undulator modules. At the moment there are no valid arguments for extending the femtosecond mode of operation below 30 nm. Figure 47 shows the evolution of the energy in the radiation pulse versus undulator length. Plots for the peak and average brilliance are presented in Figs. 48 and 49. Figures 50-58 present the expected time and spectral structure of the radiation pulse, the intensity distribution in the near zone, and the angular distribution in the far zone.

Table 4
FEL at TTF Phase 2
/ Short wavelength mode of operation /

	Units	6.4 nm	13 nm	30 nm
Electron beam				
Energy	MeV	1000	701.5	461.5
Peak current	kA		2.5	
rms bunch length	μm		50	
Bunch separation	ns		111	
Number of bunches per train	#		7200	
Repetition rate	Hz		10	
Normalized rms emittance	π mm mrad		2	
External β-function	m		4.5	
rms beam size	μm	68	80	100
rms energy spread (entrance)	MeV		1	
Undulator*				
Period	cm		2.73	
Gap	mm		12	
Peak magnetic field	T		0.495	
Coherent radiation				
Wavelength	nm	6.4	13	30
Diffraction parameter	#	21	17.6	14.3
Saturation length	m	26.2	21.2	17.8
Peak power	GW	2.8	2.5	1.8
Average power	W	40	35	27
Spot size at the undulator exit (FWHM)	μm	140	170	210
Angular divergence (FWHM)	μrad	24	35	70
Bandwidth (FWHM)	%	0.36	0.46	0.62
Pulse duration (FWHM)	fs	200	200	200
Peak flux of photons	#/sec	9×10^{25}	1.6×10^{26}	2.8×10^{26}
Average flux of photons	#/sec	1.3×10^{18}	2.3×10^{18}	4×10^{18}
Peak spectral brilliance	B**	2.4×10^{30}	8.1×10^{29}	2×10^{29}
Average spectral brilliance	B**	3.5×10^{22}	1.2×10^{22}	2.9×10^{21}
Incoherent radiation				
Average SR power	W	0.3	0.1	0.04

*Hybrid, planar undulator.
**In units of photons/sec/mrad^2/mm^2/(0.1 % bandwidth).

Table 5
FEL at TTF Phase 2
/ Long wavelength mode of operation /

	Units	30 nm	60 nm	120 nm
Electron beam				
Energy	MeV	461.5	326.3	230.5
Peak current	A		500	
rms bunch length	μm		250	
Bunch separation	ns		111	
Number of bunches per train	#		7200	
Repetition rate	Hz		10	
Normalized rms emittance	π mm mrad		2	
External β-function	m		4.5	
rms beam size	μm	100	118	141
rms energy spread (entrance)	MeV		0.2	
Undulator*				
Period	cm		2.73	
Gap	mm		12	
Peak magnetic field	T		0.495	
Coherent radiation				
Wavelength	nm	30	60	120
Diffraction parameter	#	6.4	5.4	4.5
Saturation length	m	21.5	17	14.1
Peak power	MW	345	320	270
Average power	W	25	23	20
Spot size at the undulator exit (FWHM)	μm	230	240	350
Angular divergence (FWHM)	μrad	70	125	170
Bandwidth (FWHM)	%	0.36	0.45	0.57
Pulse duration (FWHM)	ps	1	1	1
Peak flux of photons	#/sec	5.2×10^{25}	9.6×10^{25}	1.7×10^{26}
Average flux of photons	#/sec	3.8×10^{18}	6.9×10^{18}	1.2×10^{19}
Peak spectral brilliance	B**	6.5×10^{28}	2.4×10^{28}	8×10^{27}
Average spectral brilliance	B**	4.7×10^{21}	1.7×10^{21}	5.8×10^{20}
Incoherent radiation				
Average SR power	W	0.05	0.02	0.008

*Hybrid, planar undulator.
**In units of photons/sec/mrad^2/mm^2/(0.1 % bandwidth).

Table 6
FEL at TTF Phase 2
/ femtosecond mode of operation /

	Units	30 nm	60 nm	120 nm
Electron beam				
Energy	MeV	461.5	326.3	230.5
Peak current	A		1300	
rms bunch length	μm		16	
Bunch separation	ns		111	
Number of bunches per train	#		7200	
Repetition rate	Hz		10	
Normalized rms emittance	π mm mrad		6	
External β-function	m		4.5	
rms beam size	μm	173	205	244
rms energy spread (entrance)	MeV		0.2	
Undulator*				
Period	cm		2.73	
Gap	mm		12	
Peak magnetic field	T		0.495	
Coherent radiation				
Wavelength	nm	30	60	120
Diffraction parameter	#	30.9	26	21.9
Saturation length	m	27.5	20.5	15
Peak power	MW	800	530	430
Average power	W	3.2	3.2	2.7
Spot size at the undulator exit (FWHM)	μm	350	500	1400
Angular divergence (FWHM)	μrad	40	82	135
Bandwidth (FWHM)	%	0.4	0.45	0.6
Pulse duration (FWHM)	fs	55	84	88
Peak flux of photons	#/sec	1.2×10^{26}	1.6×10^{26}	2.6×10^{26}
Average flux of photons	#/sec	4.8×10^{17}	9.7×10^{17}	1.6×10^{18}
Peak spectral brilliance	B^{**}	1.3×10^{29}	4.2×10^{28}	1.2×10^{28}
Average spectral brilliance	B^{**}	5×10^{20}	2.6×10^{20}	7.6×10^{19}

*Hybrid, planar undulator.
**In units of photons/sec/mrad^2/mm^2/(0.1 % bandwidth).

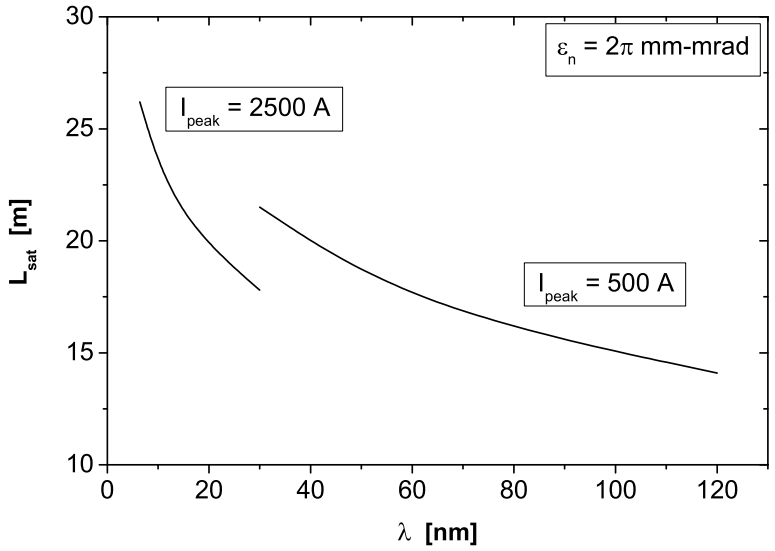


Fig. 22. *Saturation length versus radiation wavelength for FEL parameters listed in Tables 4 and 5 (normalized emittance 2π mm-mrad)*

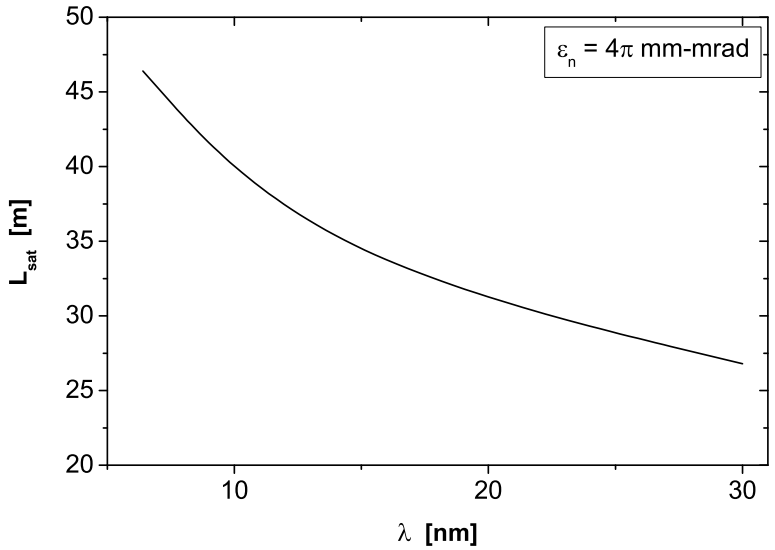


Fig. 23. *Saturation length versus radiation wavelength for FEL parameters listed in Tables 4 and 5, but with normalized emittance 4π mm-mrad*

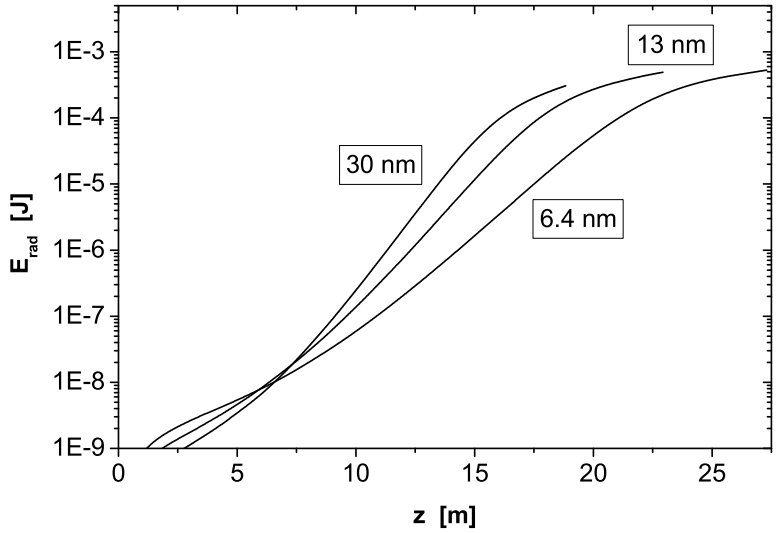


Fig. 24. *Energy in the radiation pulse versus undulator length for FEL parameters listed in Table 4 (peak beam current 2500 A, normalized emittance 2π mm-mrad)*

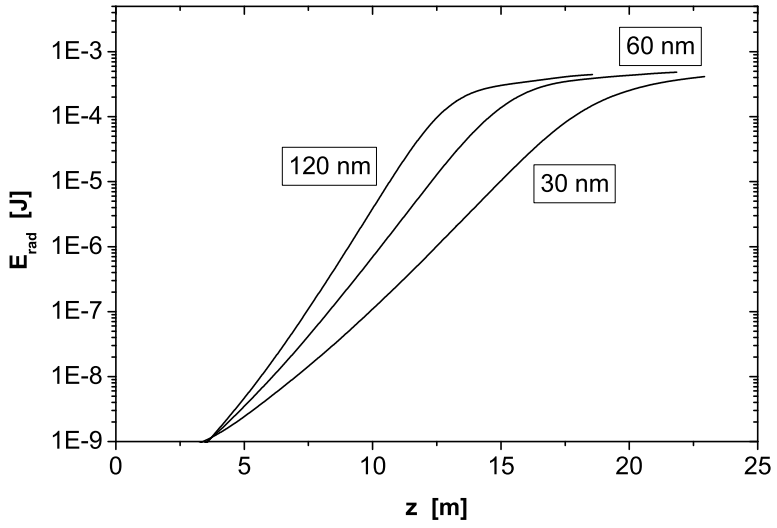


Fig. 25. *Energy in the radiation pulse versus undulator length for FEL parameters listed in Table 5 (peak beam current 500 A, normalized emittance 2π mm-mrad)*

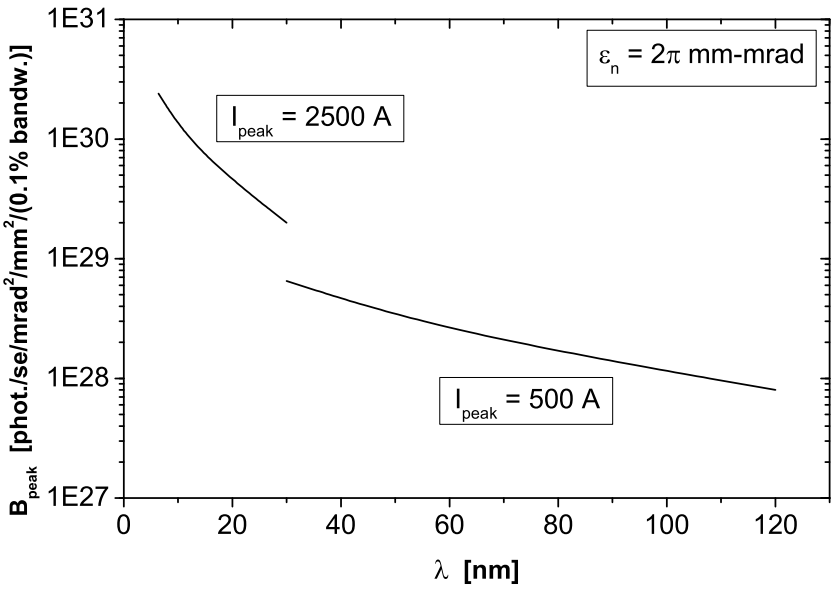


Fig. 26. *Peak brilliance for FEL parameters listed in Tables 4 and 5 (nominal parameters of electron beam, normalized emittance 2π mm-mrad)*

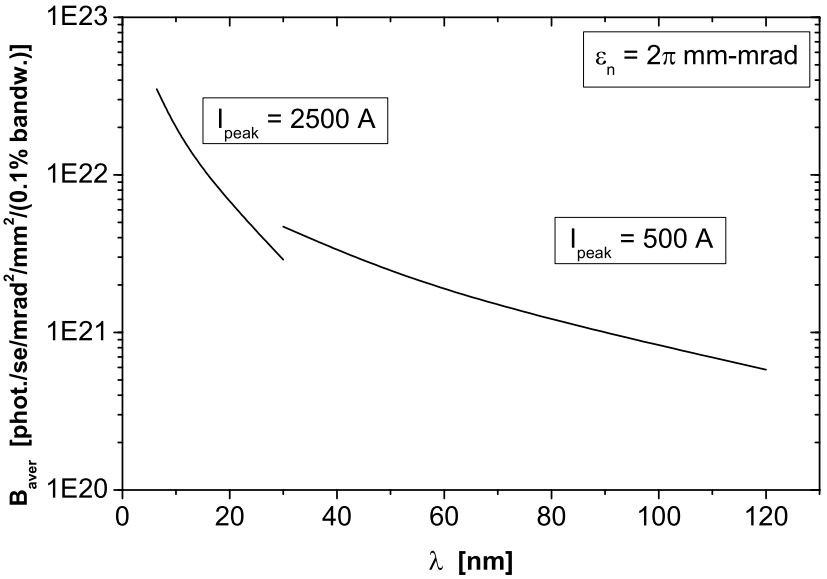


Fig. 27. *Average brilliance for FEL parameters listed in Tables 4 and 5 (nominal parameters of electron beam, normalized emittance 2π mm-mrad)*

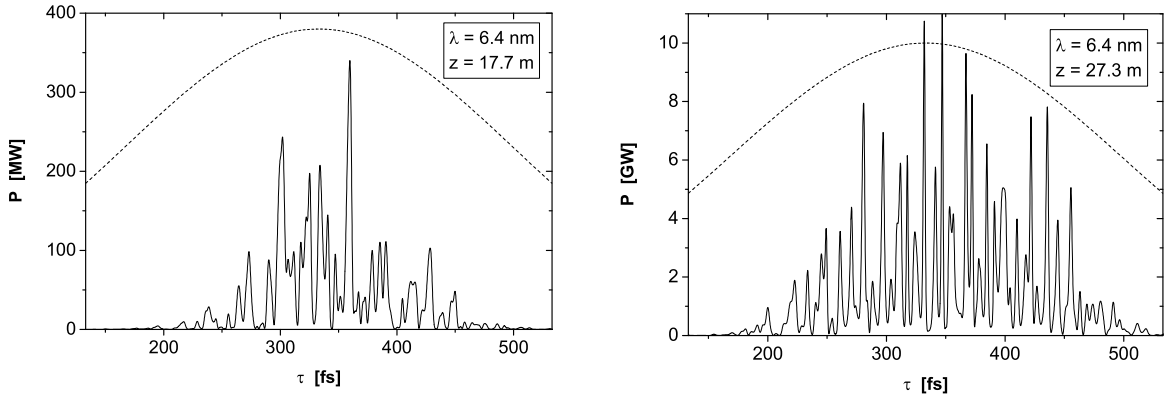


Fig. 28. *Short wavelength option at 6.4 nm: time structure of the radiation pulse. Left plot: linear regime, right plot: saturation. The dashed line represents the longitudinal profile of the electron bunch*

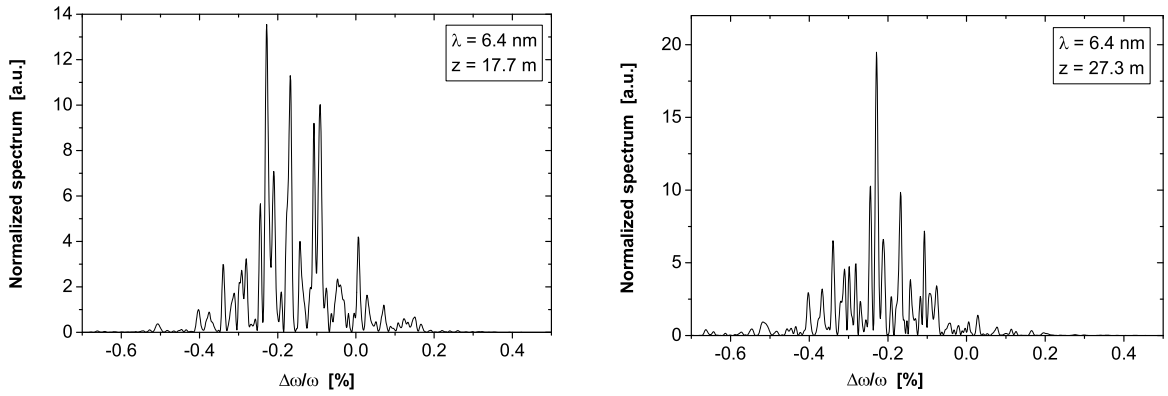


Fig. 29. *Short wavelength option at 6.4 nm: spectral structure of the radiation pulse. Left plot: linear regime, right plot: saturation.*

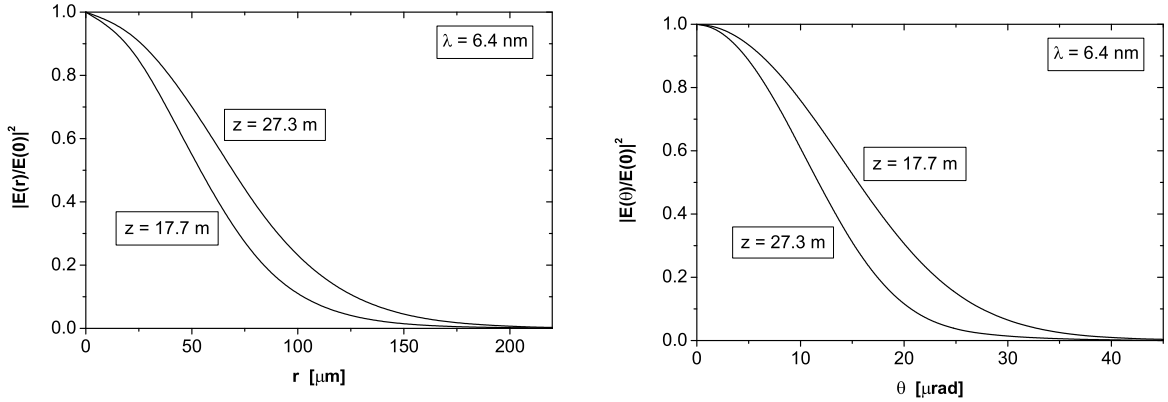


Fig. 30. *Short wavelength option at 6.4 nm: intensity distribution in the near zone (left plot) and directivity diagram of the radiation in the far zone (right plot).*

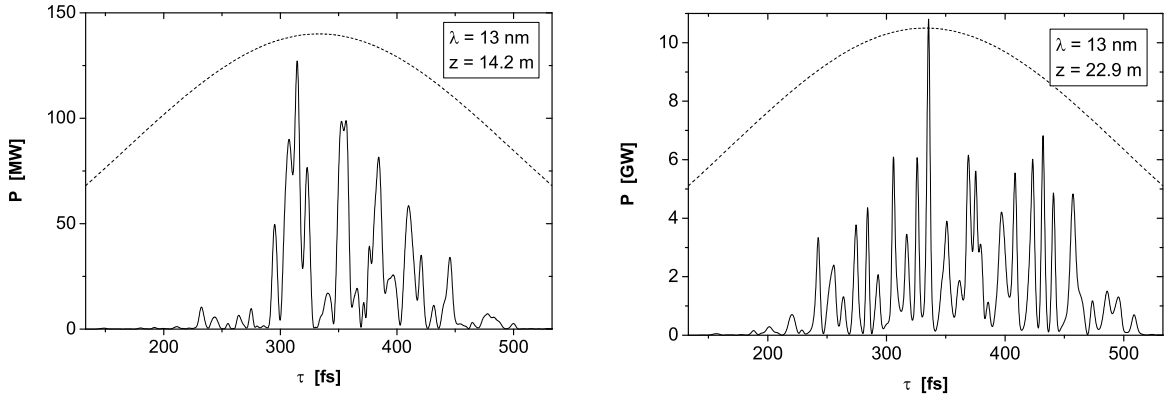


Fig. 31. *Short wavelength option at 13 nm: time structure of the radiation pulse. Left plot: linear regime, right plot: saturation. The dashed line represents the longitudinal profile of the electron bunch*

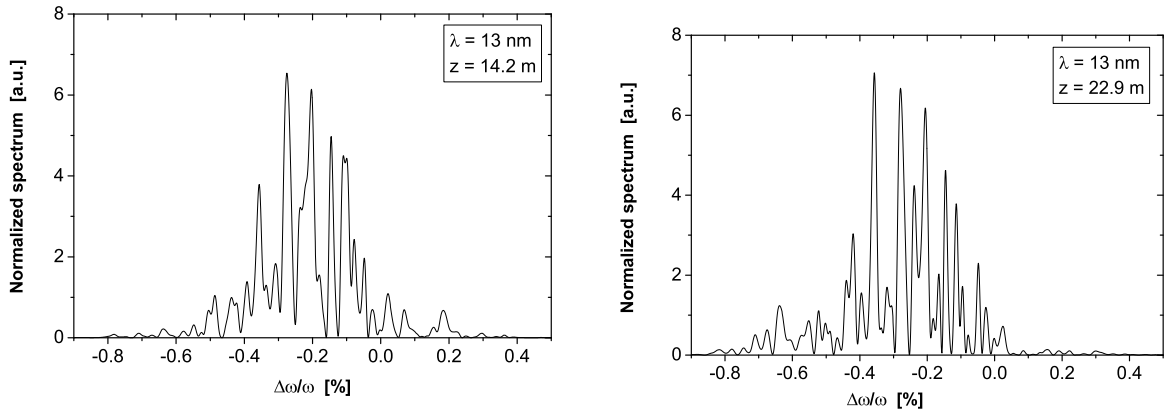


Fig. 32. *Short wavelength option at 13 nm: spectral structure of the radiation pulse. Left plot: linear regime, right plot: saturation*

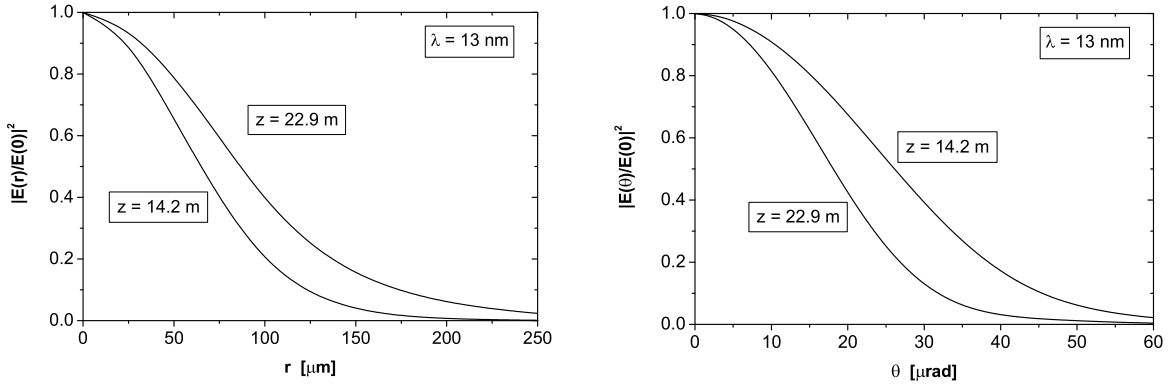


Fig. 33. *Short wavelength option at 13 nm: intensity distribution in the near zone (left plot) and directivity diagram of the radiation in the far zone (right plot)*

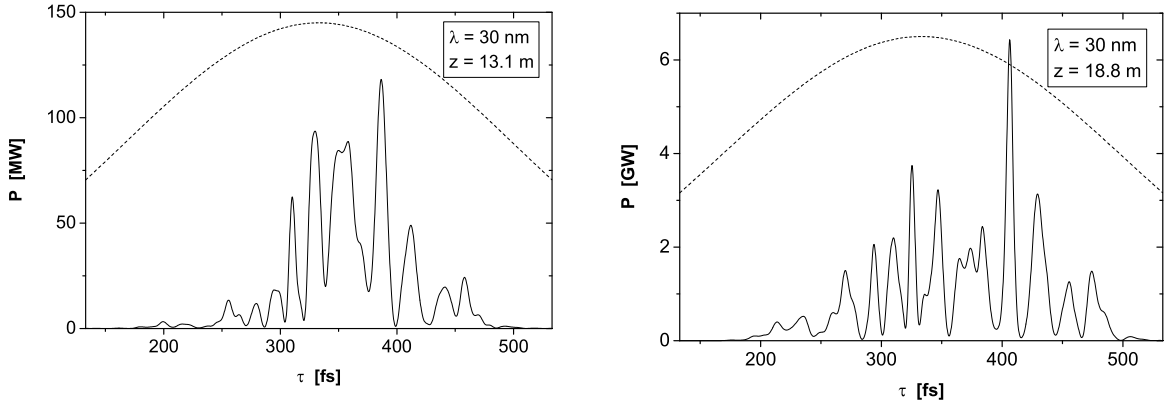


Fig. 34. *Short wavelength option at 30 nm: time structure of the radiation pulse. Left plot: linear regime, right plot: saturation. The dashed line represents the longitudinal profile of the electron bunch*

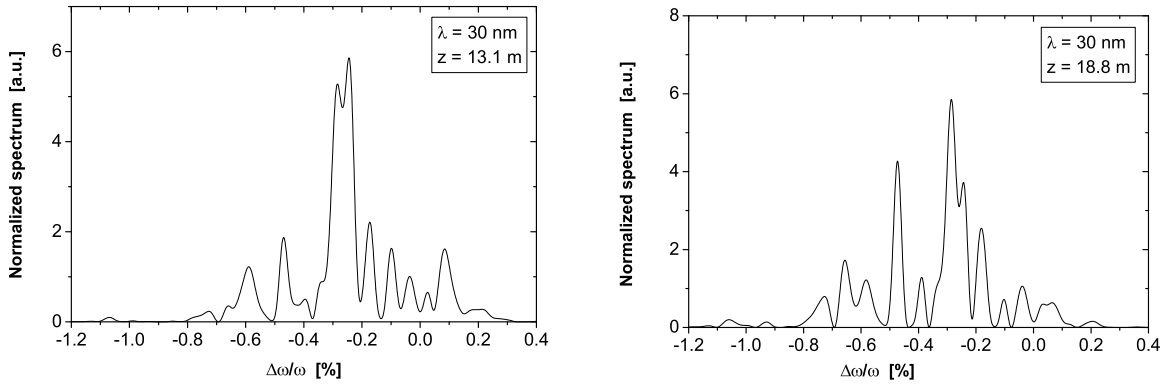


Fig. 35. *Short wavelength option at 30 nm: spectral structure of the radiation pulse. Left plot: linear regime, right plot: saturation*

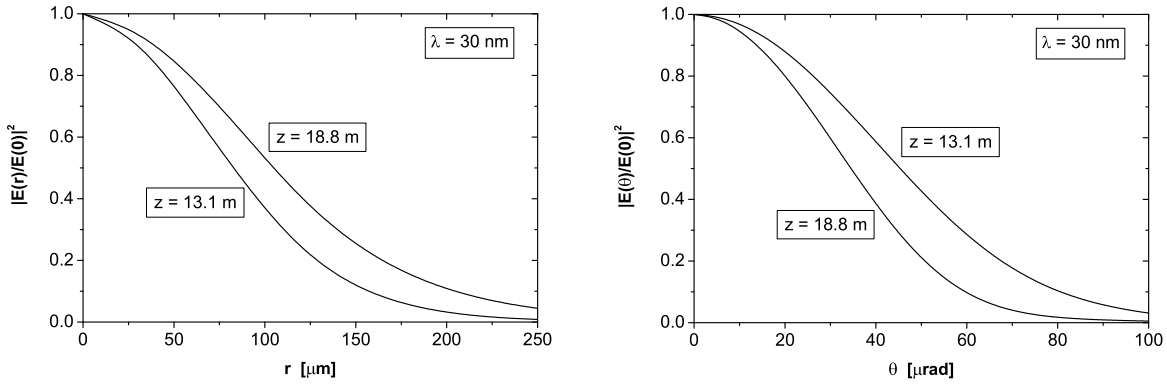


Fig. 36. *Short wavelength option at 30 nm: intensity distribution in the near zone (left plot) and directivity diagram of the radiation in the far zone (right plot)*

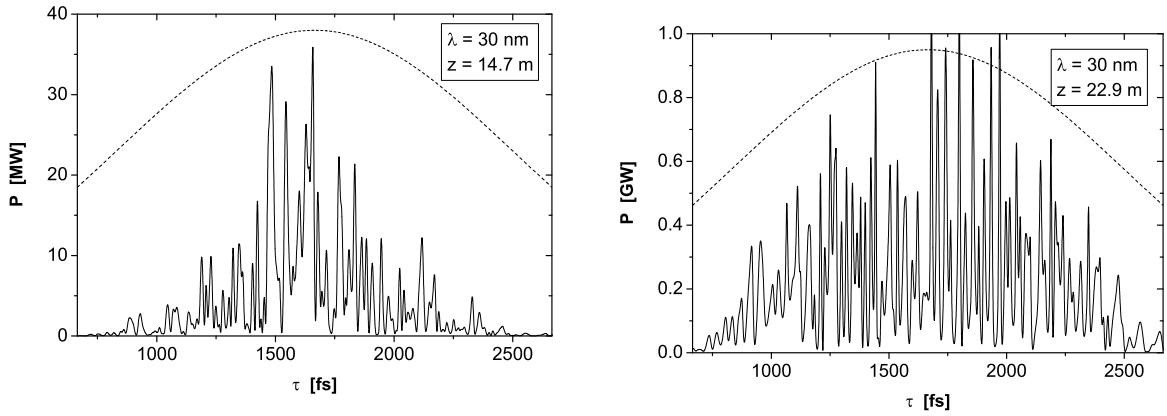


Fig. 37. *Long wavelength option at 30 nm: time structure of the radiation pulse. Left plot: linear regime, right plot: saturation. The dashed line represents the longitudinal profile of the electron bunch*

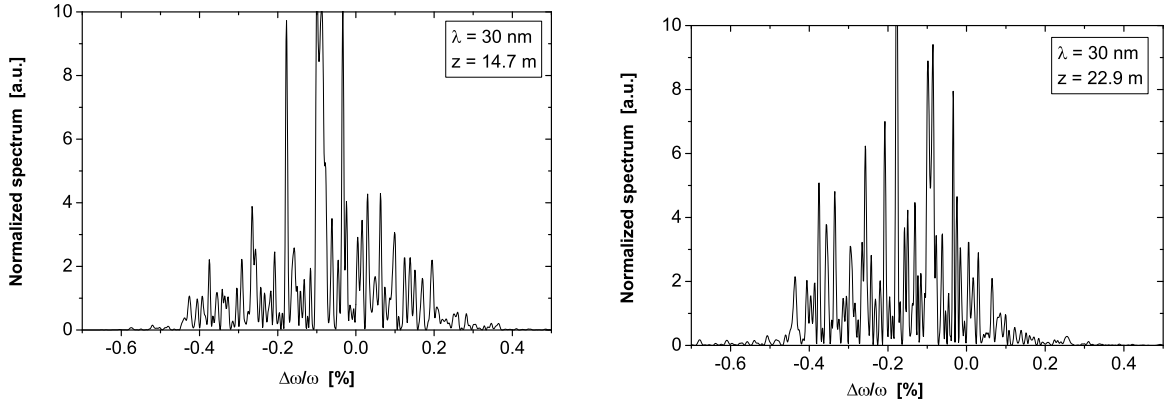


Fig. 38. *Long wavelength option at 30 nm: spectral structure of the radiation pulse. Left plot: linear regime, right plot: saturation*

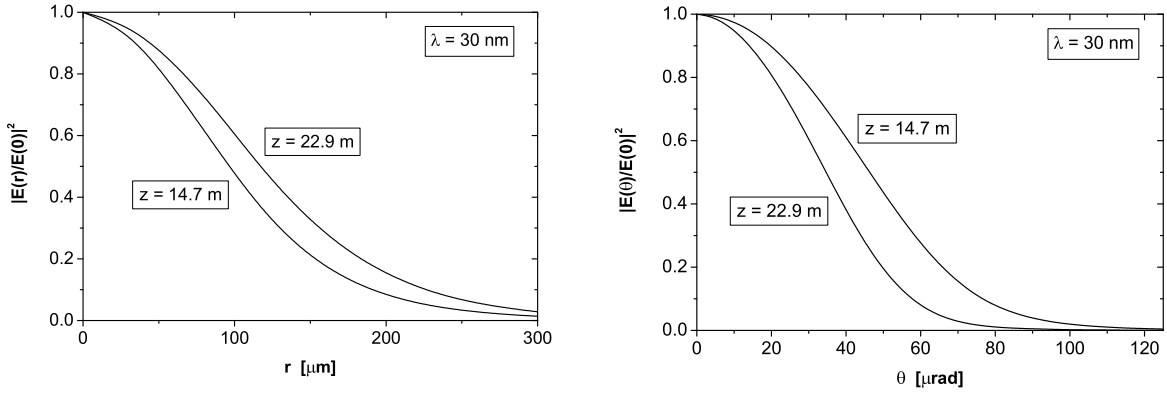


Fig. 39. *Long wavelength option at 30 nm: intensity distribution in the near zone (left plot) and directivity diagram of the radiation in the far zone (right plot)*

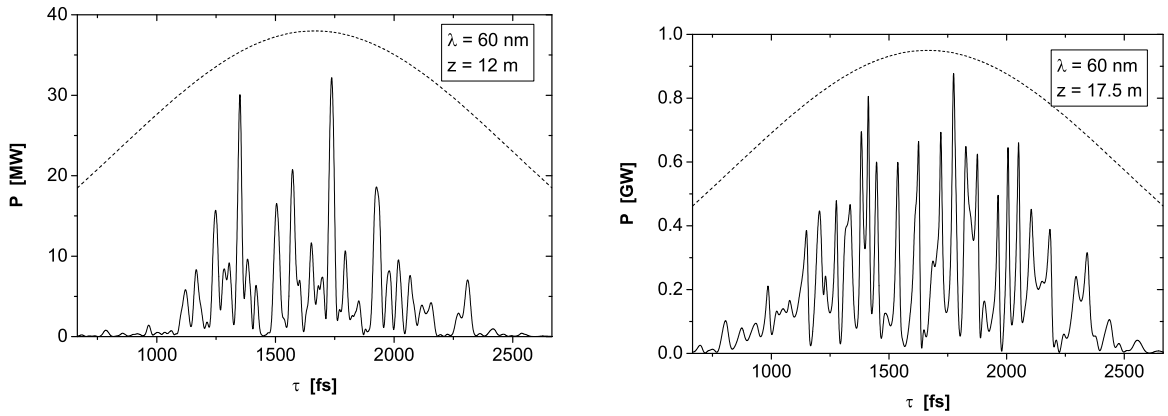


Fig. 40. *Long wavelength option at 60 nm: time structure of the radiation pulse. Left plot: linear regime, right plot: saturation. The dashed line represents the longitudinal profile of the electron bunch*

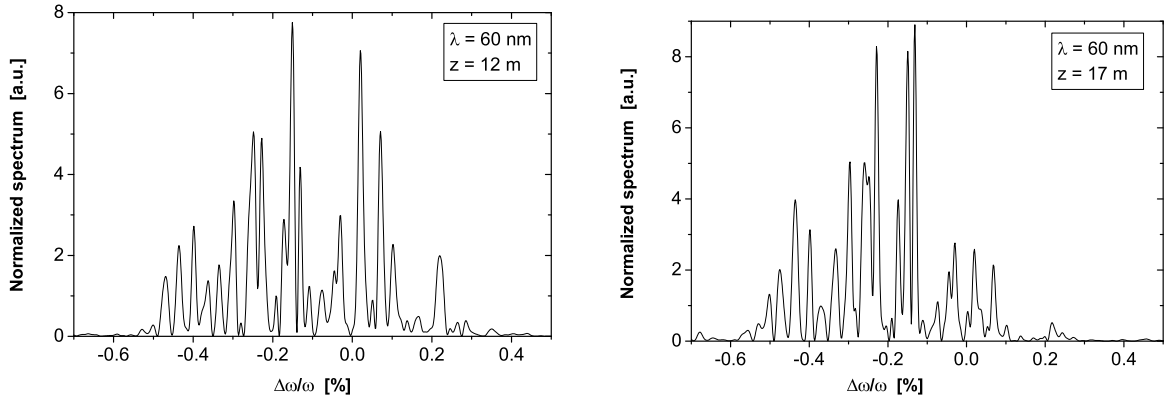


Fig. 41. *Long wavelength option at 60 nm: spectral structure of the radiation pulse. Left plot: linear regime, right plot: saturation*

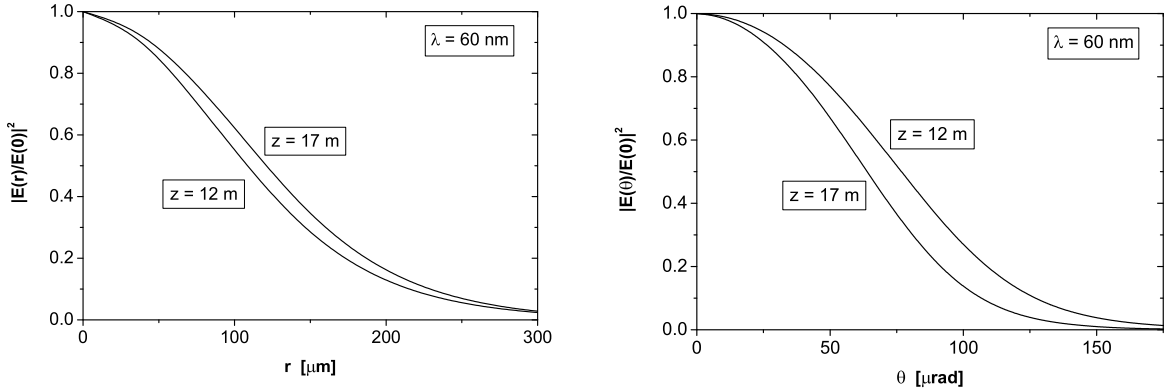


Fig. 42. *Long wavelength option at 60 nm: intensity distribution in the near zone (left plot) and directivity diagram of the radiation in the far zone (right plot)*

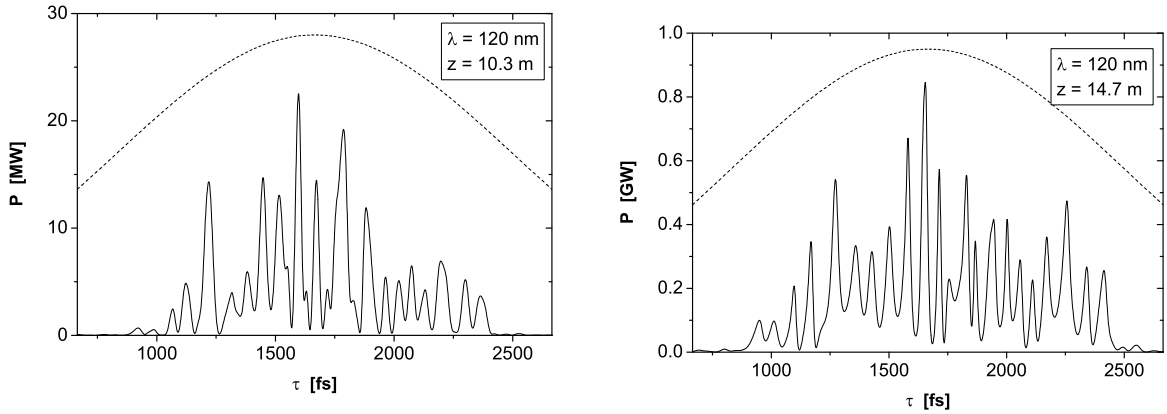


Fig. 43. *Long wavelength option at 120 nm: time structure of the radiation pulse. Left plot: linear regime, right plot: saturation. The dashed line represents the longitudinal profile of the electron bunch*

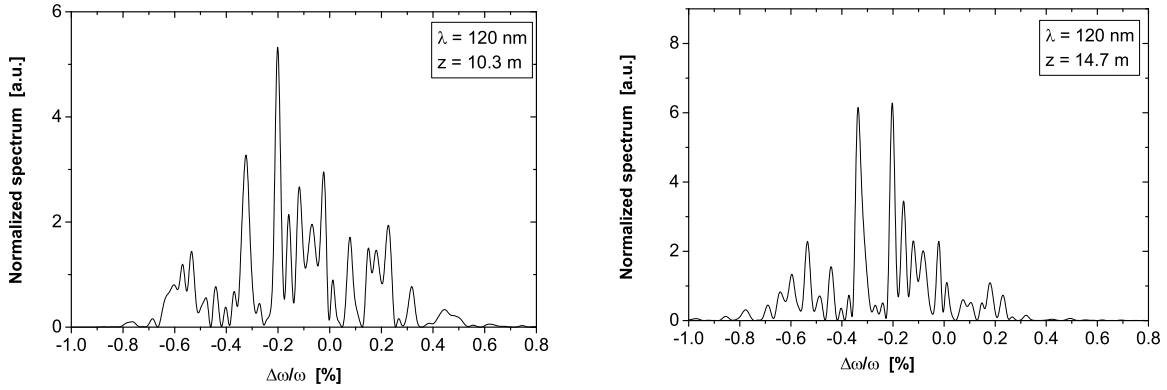


Fig. 44. *Long wavelength option at 120 nm: spectral structure of the radiation pulse. Left plot: linear regime, right plot: saturation*

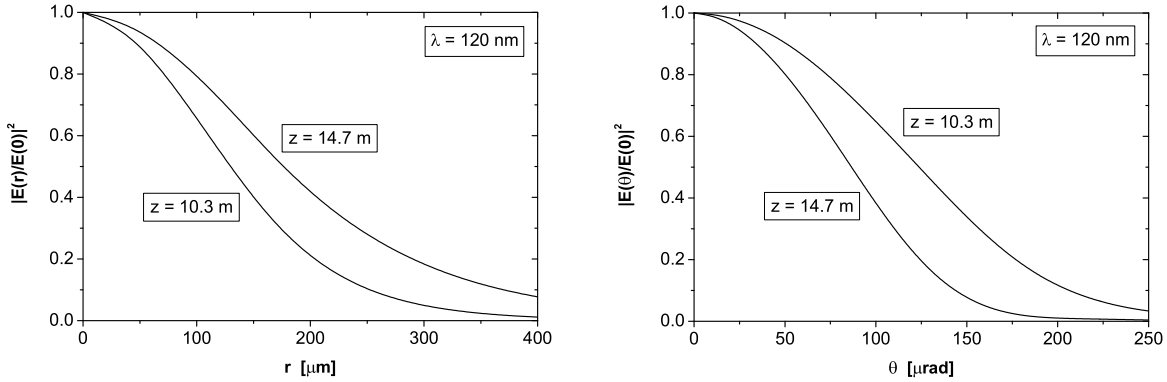


Fig. 45. *Long wavelength option at 120 nm: intensity distribution in the near zone (left plot) and directivity diagram of the radiation in the far zone (right plot)*

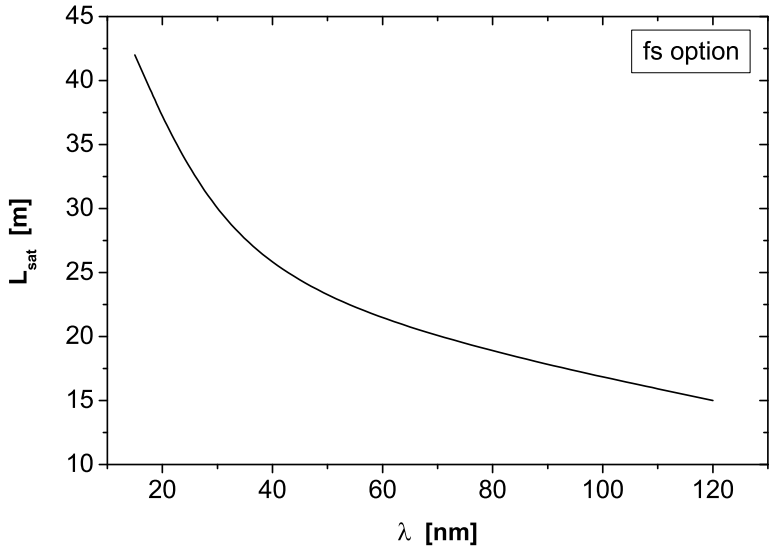


Fig. 46. *Saturation length versus radiation wavelength for FEL parameters listed in Table 6 (femtosecond mode of operation)*

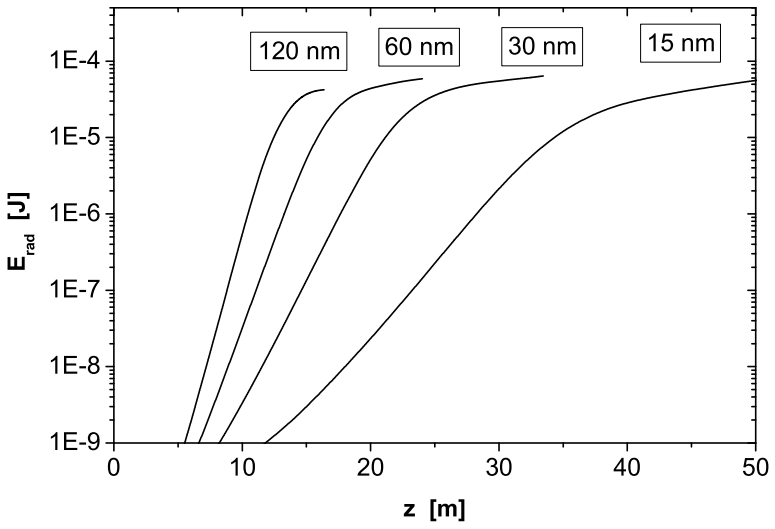


Fig. 47. *Energy in the radiation pulse versus undulator length for FEL parameters listed in Table 6 (femtosecond mode of operation)*

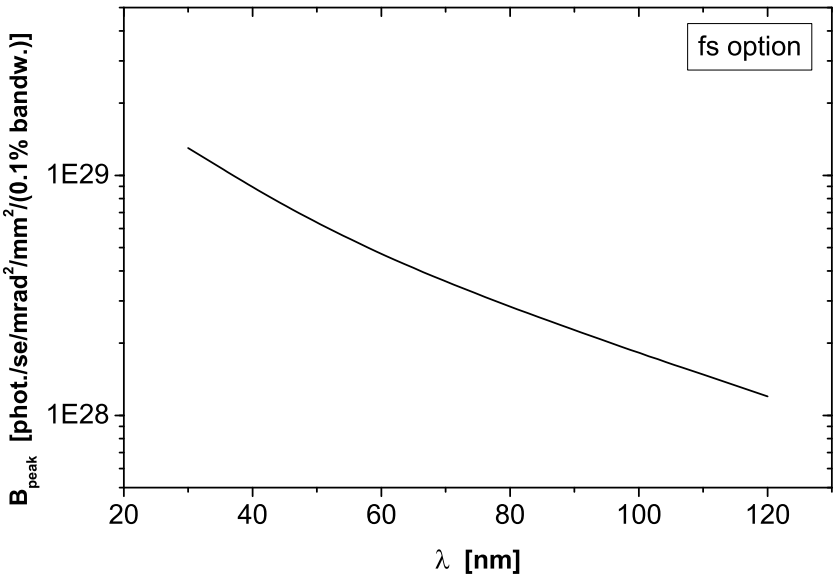


Fig. 48. *Peak brilliance for FEL parameters listed in Table 6 (femtosecond mode of operation)*

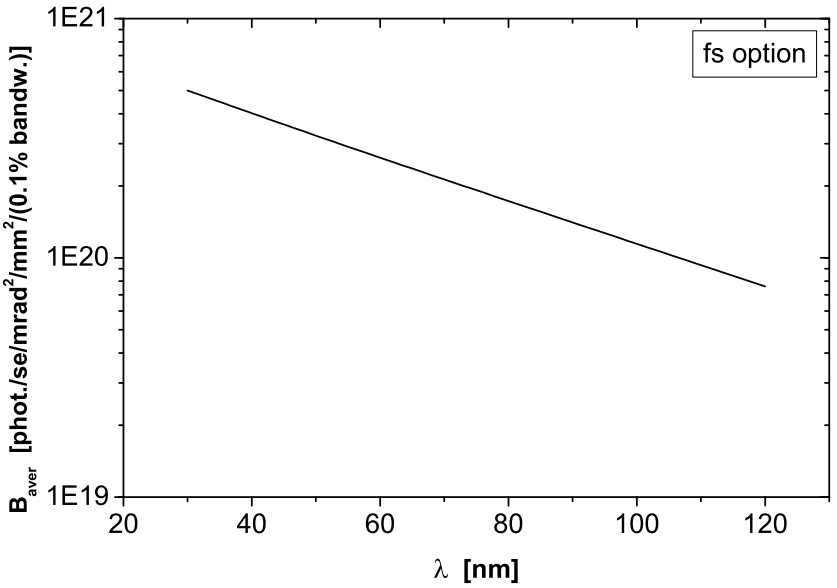


Fig. 49. *Average brilliance for FEL parameters listed in Table 6 (femtosecond mode of operation)*

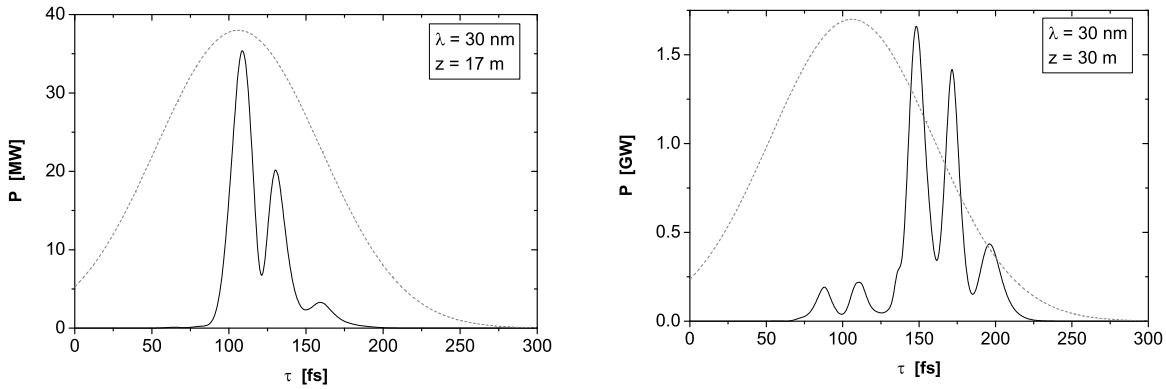


Fig. 50. *Femtosecond option at 30 nm: time structure of the radiation pulse. Left plot: linear regime, right plot: saturation. The dashed line represents the longitudinal profile of the electron bunch*

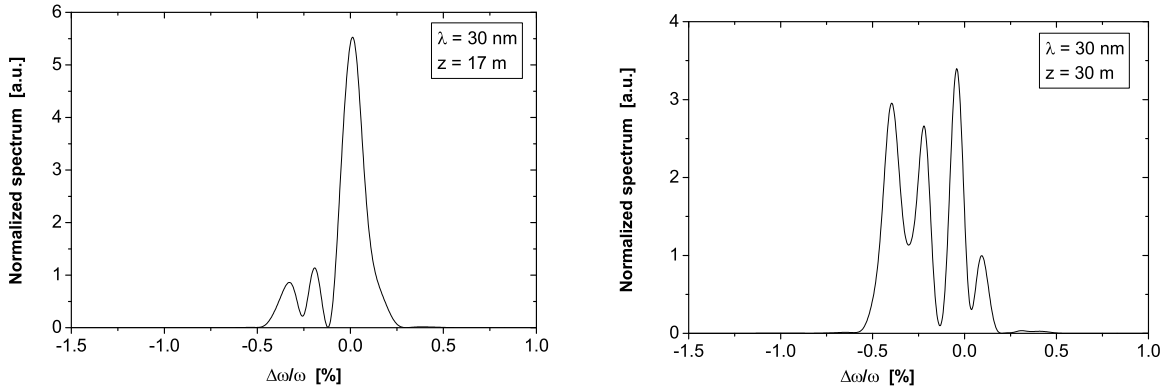


Fig. 51. *Femtosecond option at 30 nm: spectral structure of the radiation pulse. Left plot: linear regime, right plot: saturation*

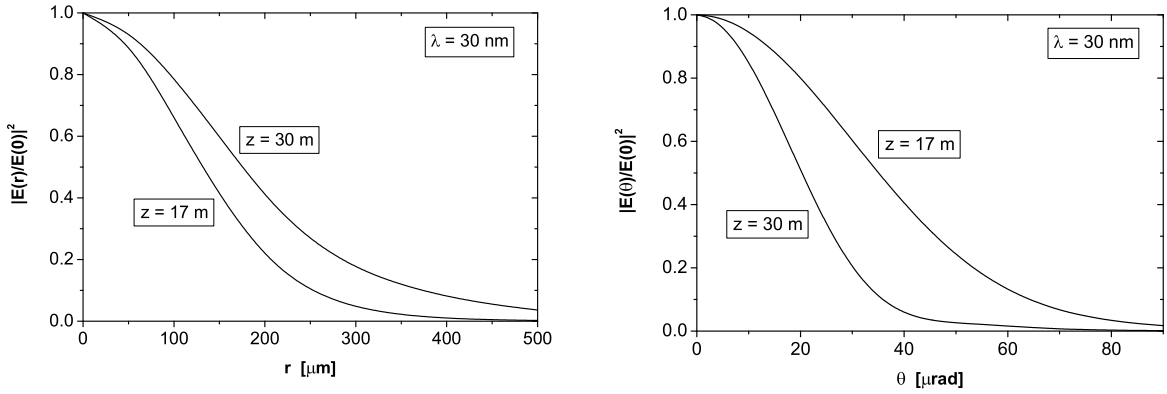


Fig. 52. *Femtosecond option at 30 nm: intensity distribution in the near zone (left plot) and directivity diagram of the radiation in the far zone (right plot)*

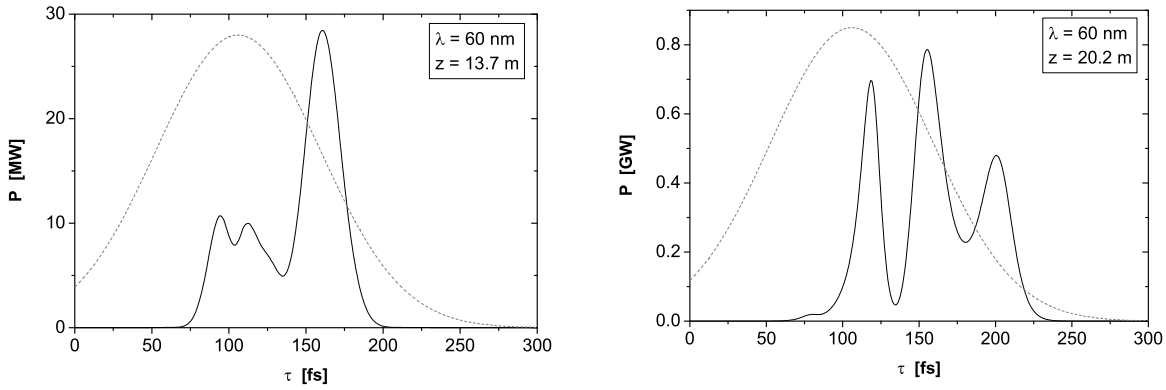


Fig. 53. *Femtosecond option at 60 nm: time structure of the radiation pulse. Left plot: linear regime, right plot: saturation. The dashed line represents the longitudinal profile of the electron bunch*

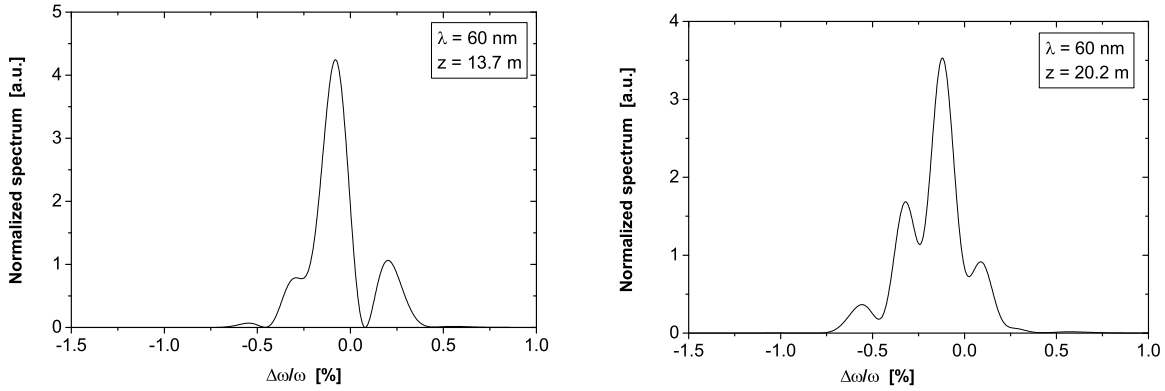


Fig. 54. *Femtosecond option at 60 nm: spectral structure of the radiation pulse. Left plot: linear regime, right plot: saturation*

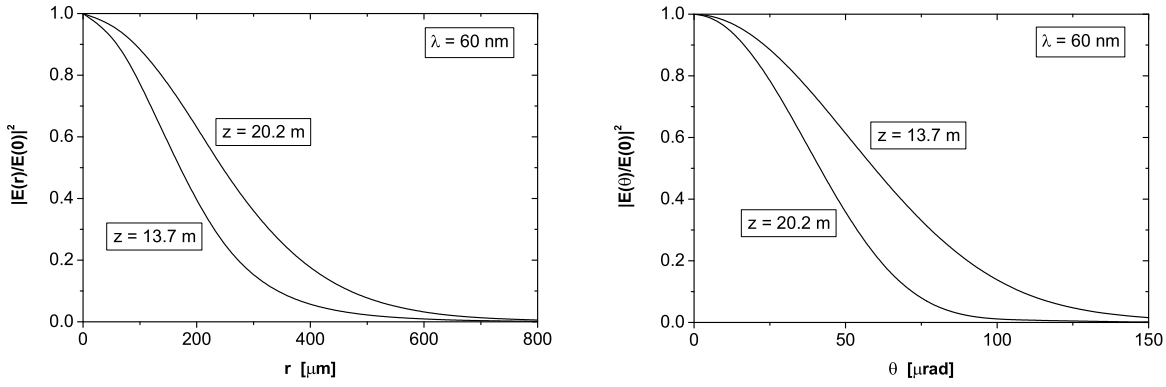


Fig. 55. *Femtosecond option at 60 nm: intensity distribution in the near zone (left plot) and directivity diagram of the radiation in the far zone (right plot)*

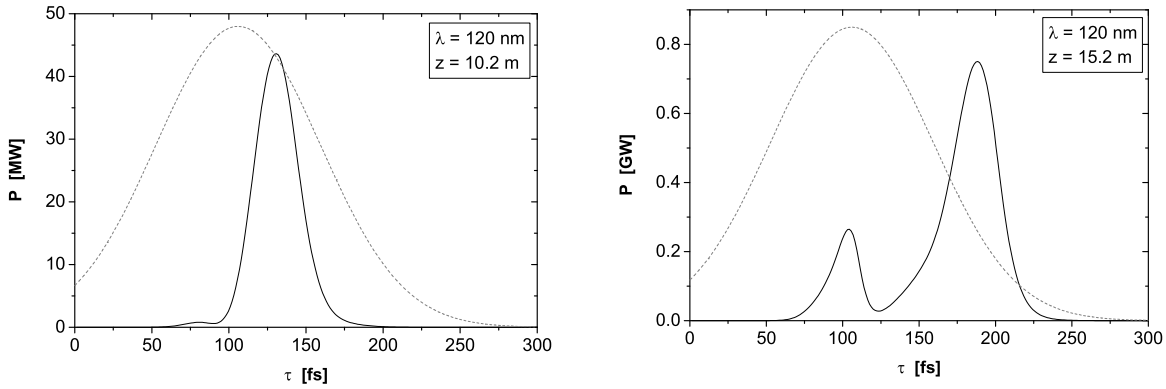


Fig. 56. *Femtosecond option at 120 nm: time structure of the radiation pulse. Left plot: linear regime, right plot: saturation. The dashed line represents the longitudinal profile of the electron bunch*

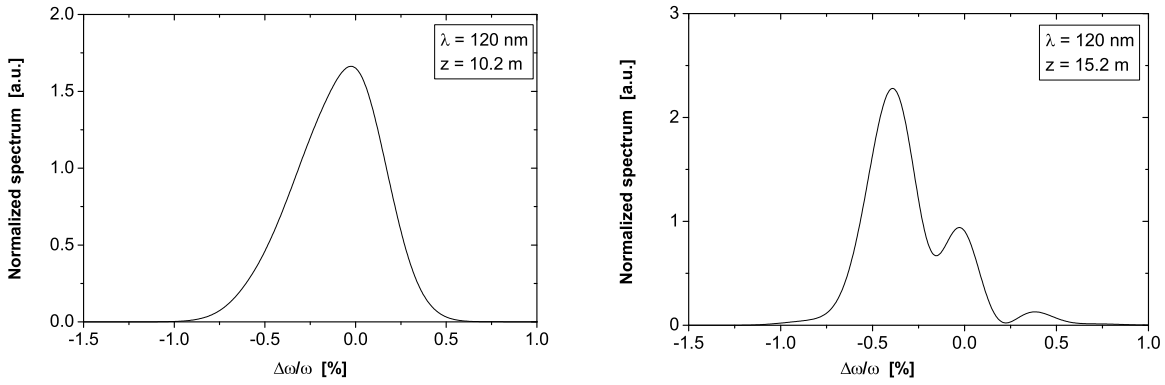


Fig. 57. *Femtosecond option at 120 nm: spectral structure of the radiation pulse. Left plot: linear regime, right plot: saturation*

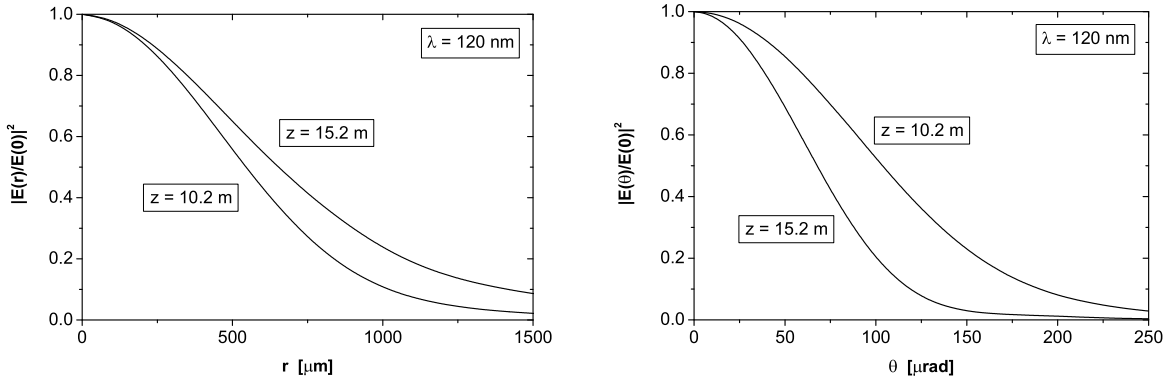


Fig. 58. *Femtosecond option at 120 nm: intensity distribution in the near zone (left plot) and directivity diagram of the radiation in the far zone (right plot)*

References

[1] A VUV Free Electron Laser at the TESLA Test Facility at DESY, Conceptual Design report, Deutsches Elektronen-Synchrotron, DESY, TESLA-FEL 95-03, DESY, Hamburg, Germany

[2] J. Fraser, R. Sheffield, *Nucl. Instr. Meth.* **A285**, 71 (1986)

[3] B. E. Carsten, *Nucl. Instr. Meth.* **A285**, 313 (1989)

[4] X. Qiu et al., *Phys. Rev. Lett.* **76** (20), 3723 (1996)

[5] D. Dwersteg, K. Flöttmann, J. Sekutovicz, Ch. Stolzenburg, *Nucl. Instr. Meth.* **A393**, 93 (1997)

[6] D. Sertore, S. Schreiber, F. Stephan, K. Flöttmann, K. Zapfe, *Nucl. Instr. Meth.* **A445**, 422 (2000)

[7] I. Will, A. Liero D. Merins, W. Sander, *IEEE Journ. Quan. Electronics* **34**, 2020 (1998)

[8] M. Ferrario, K. Flöttmann, T. Limberg, Ph. Piot, B. Grigoryan, Conceptual Design of the TESLA XFEL Photoinjector, TESLA-FEL Report 2001-03, DESY (2001)

[9] M. Geitz, et al. “bunch compressor II at TTF”, Proceedings PAC’99 New-York, 2507 (1999)

[10] A. Loulergue, A. Mosnier, “A Simple S-Chicane for the final bunch compressor of TTF-FEL”, Proceedings EPAC2000 Vienna, 752 (2000)

[11] K. Flöttmann, *Astra User Manual*

[12] M. Borland, “Elegant: A flexible sdds-compliant code for accelerator simulation”, LS-287, Argonne National Laboratory (2000)

[13] M. Dohlus, A. Kabel, T. Limberg, *Nucl. Instr. Meth.* **A445**, 338 (2000)

[14] A. Novokhaski, M. Timm, T. Weiland, “Single bunch energy spread in the TESLA cryomodule”, TESLA 99-16, DESY (1999)

[15] K. Flöttmann, B. Grygorian, Ph. Piot, “Injector upgrade for the TTF user facility: Design and performance study”, TESLA-FEL-2002-04, DESY (2002)

[16] J.S. Nodvick, D.S. Saxon, *Phys. Rev.* **96**, 180 (1954)

[17] E. Saldin, E. Schneidmiller, M. Yurkov *Nucl. Instr. Meth.* **A 398**, 373 (1997)

[18] V. Balandin, N. Golubeva, M. Körfer, Studies of beam optics in the collimation system for the TTF FEL at DESY, Proceedings FEL2001, Darmstadt, Germany

[19] H. Henschel, M. Körfer, F.Wulf, Fibre Optic Radiation Sensing System for TESLA, TESLA Report 2000-26, DESY, 2000

[20] E. Janata, M. Körfer, Radiation Detection by Cerenkov Emission in Optical Fibers at TTF, TESLA Report 2000-27, DESY, 2000

[21] P. Catravas, W.P. Leemans, Proceedings PAC99, 2111 (1999)

[22] G.A. Krafft, AIP conference proceedings **367**, 46 (1995)

[23] Ph. Piot, G.A. Krafft, D.R. Douglas, Proceedings EPAC2000, 1543 (2000)

[24] P. Emma, J. Frisch, P. Krejcik, “A transverse RF deflecting structure for bunch length measurement and phase space diagnostics”, LCLS-TN-00-12, SLAC (2000)

[25] D.X. Wang, G.A. Krafft, C.K. Sinclair, *Phys. Rev.* **E57**, 2293 (1998)

[26] R. Lai, A.J. Sievers, *Phys. Rev.* **E52** (2), 4576 (1995)

[27] R. Follath, F. Senf, W. Gudat, J. Synchrotron Rad. 5,769 (1998)

[28] S. Schreiber, I. Will, D. Sertore, A. Liero, W. Sandner, Nucl. Instr. Meth. A 445, 427 (2000)

[29] J. Andruskow et. al. Phys. Rev. Lett. 85 (2000) 3825

[30] W. Brefeld et. al, ”, Nucl. Instr. and Methods A375 (1996), 295

[31] J. Feldhaus, E.L. Saldin, J.R. Schneider, E.A. Schneidmiller, M.V.Yurkov, ” Possible application of X-ray optical elements for reducing the spectral bandwidth of an X-ray SASE FEL”, Opt. Commun. 140, 341-352 (1997)

[32] J. Pfüger, Y. M. Nikitina, ”Planar Undulator Schemes with strong focusing Properties for the VUV-FEL at the TESLA Test Facility”, Nucl. Instr. and Methods A381 (1996), 554

[33] See: http://www-hasylab.desy.de/facility/fel/main.htm for a compact description of the undulator for Phase I

[34] J. Pflüger, U. Hahn, HASYLAB Annual Report 1999 p 89 ff *

[35] J. Pflüger, B. Faatz, HASYLAB Annual Report 1998 p 104 ff *

[36] U. Hahn, HASYLAB Annual Report 1998 p 110 ff *

[37] U. Hahn, P.K. den Hartog, J. Pflüger, M. Rüter, G. Schmidt, E.M. Trakhtenberg, ”Design and Performance of the Vacuum Chambers for the Undulator of the VUV-FEL at the TESLA Test Facility”, Nucl. Instr. and Methods A445 (2000), 442

[38] B. Faatz, J. Pflüger, HASYLAB Annual Report 2000 p 89 ff , Proceedings of the FEL 2000 Aug. 13-18, 2000 Durham, North Carolina, USA, in Press *

[39] P. Castro, TTF FEL Beam-based Alignment by Dispersion Correction Using Micado Algorithm, TESLA FEL report 1997-04, DESY, Hamburg.

[40] K. Flöttmann, B. Faatz, E. Czuchry and J. Rossbach, Nucl. Instr. Meth. A416 (1998) 152.

[41] B. Faatz, J. Pflüger, Yu.M. Nikitina, Nucl. Instr. Meth. A393 (1997) 380.

[42] J. Pflüger, H. Lu, T. Teichmann, Nucl. Instr. Meth. A429 (1999) 386.

[43] J. Pflüger, P. Gippner, A. Swiderski, T. Vielitz, Magnetic characterization of the Undulator for the VUV-FEL at the TESLA Test Facility, prsented at the International Free Electron Laser Conference, August 23-26, 1999, DESY, Hamburg, Germany.